GEORG-AUGUST-UNIVERSITÄT
GÖTTINGEN

Fakultät für
Physik

Bachelor's Thesis

Studien von Streuung und hochenergetischer Energiedeposition in Mikrometervolumina mittels des DEPFET Detektors

Study of Straggling and Extreme Cases of Energy Deposition in Micron Scale Silicon Volumes using the DEPFET Detector

prepared by

Fabian Wilk

from Kassel

at the II. Institute of Physics

Thesis Period:	16th April 2012 until 23rd July 2012
Thesis Number:	II. Physik-UniGö-BSc-2012/05
Supervisor:	Dipl. Phys. Benjamin Schwenker
First Referee:	Prof. Dr. Ariane Frey
Second Referee:	P.D. Dr. Jörn Grosse-Knetter

Abstract

The ***De**pleted **P**-channel **F**ield-**E**ffect **T**ransistor* detector is a pixel detector type currently under development. In high energy physics, pixel detectors measure space points along the trajectory of charged particles. They determine the spatial position by measuring the charges created as a result of interactions with the passing particle. Thus the detector's signals can be used to determine the energy deposited by the particle in single pixels of a pixel matrix.

The development of a new detector raises the question whether our simulation models can accurately describe the physical processes – like ionisation and scattering – taking place during operation. The thesis aims to validate one of the current Monte-Carlo simulations (based on the `Geant4` simulation package) of high energy straggling processes using experimental data of a test beam run of DEPFET modules. This is done by calculating the spatial distribution of the electron/hole pairs created in extreme cases of ionisation and using this distribution for comparison and analysis of the data samples.

Keywords: DEPFET, Belle II, Ionisation, Delta Electrons, `Geant4`, Straggling, Scattering

Zusammenfassung

Der ***De**pleted **P**-channel **F**ield-**E**ffect **T**ransistor* Detektor ist ein Pixel Detektor, welcher momentan für eine professionelle Anwendung entwickelt wird. Im Kontext der Hochenergiephysik messen Pixel Detektoren Spurpunkte entlang der Trajektorie von geladenen Teilchen. Dies geschieht durch Messung der Signalladungen, welche vom zu messenden Teilchen durch Interaktion erzeugt werden. Das Detektorsignal erlaubt somit die Bestimmung der deponierten Energie mittels einer Pixelmatrix, d. h. es handelt sich um eine ortsaufgelöste Messung.

Bei der Detektorentwicklung stellt sich die Frage, ob die verwendeten Simulationsmodelle die physikalischen Prozesse welche auftreten – wie z. B. Ionisation und Streuung – korrekt beschreiben. Im Rahmen dieser Arbeit soll eine gängige Monte-Carlo Simulation (basierend auf `Geant4`) ob ihrer Übereinstimmung mit experimentellen Daten überprüft werden. Dabei werden experimentelle Daten, welche in einer Testumgebung mit Hilfe des DEPFET Detektors gewonnen worden sind, verwendet. Im Speziellen soll dabei die räumliche Verteilung von Signalladungen in extremen Fällen von Ionisation rekonstruiert werden und die resultierenden Verteilungen von Experiment und Simulation sollen verglichen werden.

Stichwörter: DEPFET, Belle II, Ionisation, Delta Elektronen, `Geant4`, Streuung

Contents

1. Introduction

In this thesis we will analyse the behaviour of ionisation products in cases of extreme energy deposition. This is done by analysing data taken from test runs of a new detector type; the reconstruction of highly energetic ionisation products poses the main goal of the thesis. Furthermore the analysis is performed on a sample of simulated data to evaluate the performance of the simulation when compared to experimental data.

Chapter 2 provides the required theoretical background of interaction processes for the relevant energy scale with special emphasis on the ionisation products. The process of multiple scattering, which is of utmost importance for low energy particles traversing an absorber, is presented. Furthermore a method for analysing the asymmetric probability density functions of the energy loss distributions is discussed.
The DEPFET detector, which was used to measure the ionisation processes, is presented in chapter 3. This detector, which is currently under development for large scale application in the upcoming Belle II upgrade, has a very high spatial and energy resolution. It is due to the exquisite attributes of the DEPFET detector that the analysis performed in the thesis is possible.
In chapter 4 the experiment, in which the analysed data was measured, is presented. The different detector modules and their properties are presented among the experiment's setup. Furthermore the reconstruction chain which was applied to the data is described. Understanding the reconstruction process is crucial because this allows to understand the problems highly energetic ionisation products pose in a live research environment.
The elementary physics model used by the simulation engine has already been presented in chapter 2, however, a full simulation must further include a detector simulation stage which is explained in detail in chapter 5. Furthermore we present the simulation characteristics, calibrate the simulated data to the experimental data and perform a simple cross check of the compliance of the experimental and simulated data.
Chapter 6 summarises the reconstruction methods and gives detailed explanation about the problems of a reconstruction and possible solutions. Furthermore typical behaviour of highly energetic ionisation products, as found while working on this thesis, is presented.
The analysis criteria and methods are presented in chapter 7. Furthermore the results of

these analysis criteria is presented and the compliance of experimental and simulated data in regard to highly energetic ionisation products is evaluated.
Finally in chapter 8 a conclusion is drawn. We present the results achieved in this thesis and the flaws remaining in the analysis. Furthermore an outlook is given and possible future developments and analysis enhancements are presented.

2. Interactions of Charged Particles with Matter

The detection of particles is done by measuring the occurrence and intensity of the interactions between particles and the detector matter [1–6]. Most detection techniques use the electromagnetic interaction between charged particles and matter, which is suitable due to its large cross section.

2.1. Straggling of Heavy Charged Particles

A particle which traverses matter continuously loses energy in numerous individual COULOMB interactions (or scattering processes) with the matter. One can calculate the differential single collision cross section $\sigma(\beta\gamma, E)$ which is a measure for the probability that a particle with kinetic variables[1] $\beta\gamma$ interacts with an atom and transfers the energy E. Furthermore one can relate the total cross section σ_t to the total macroscopic cross section Σ_t via

$$\underbrace{\int_{E_{\min}}^{E_{\max}} \Sigma(\beta\gamma, E)\,\mathrm{d}E}_{=\Sigma_t(\beta\gamma)} = n \cdot \underbrace{\int_{E_{\min}}^{E_{\max}} \sigma(\beta\gamma, E)\,\mathrm{d}E}_{=\sigma_t(\beta\gamma)},$$

where n is the atomic density,[2] $E_{\min}$ is a lower cutoff value which is $\sim 10\,\mathrm{eV}$ and $E_{\max}$ is the maximum energy transfer. The macroscopic cross section is a measure for the number of interactions per unit length; one can calculate the number of collisions N_c per track segment of length x using the relation

$$N_c = x \cdot \Sigma_t(\beta\gamma)\ .$$

The number of collisions per track segment of length x is POISSON distributed with mean $x \cdot N_c$. One can calculate the distribution function of the energy loss of a single collision using

---

1 $\beta := \frac{v}{c}$ is the particle's velocity in units of the speed of light, $\gamma := \frac{1}{\sqrt{1-\beta^2}}$ is the LORENTZ-factor.

2 Which is defined as $n := \frac{N_{\mathrm{av}}\rho}{A}$ where N_{av} is AVOGADRO's constant, ρ is the matter's density and A its atomic number.

the relation

$$\Phi\left(\beta\gamma, E\right) = \frac{\int_{E_{\min}}^{E} \frac{\mathrm{d}\sigma(\beta\gamma, E')}{\mathrm{d}E'} \mathrm{d}E'}{\int_{E_{\min}}^{E_{\max}} \frac{\mathrm{d}\sigma(\beta\gamma, E')}{\mathrm{d}E'} \mathrm{d}E'} \,,$$

where the denominator is a normalisation coefficient.

2.1.1. The Straggling Function

The probability density function (PDF) $f\left(\Delta, x\right)$ – called **straggling function** – of the energy loss Δ per track segment of length x is given as sum over the single energy losses, i. e.

$$f\left(\Delta, x\right) = \sum_{i=1}^{N} E_i \,,$$

where N is sampled from the POISSON distribution with mean N_c and E_i is sampled from Φ. Signals measured by a pixel detector are comprised of numerous signal charges deposited in a certain volume. The measured signal is closely related to the straggling function of the process. The variation of the measured signal for particles of equal properties and energy is a result of the width of the distribution defined by the straggling function.

2.1.2. Approximated Straggling Functions

The straggling function can be approximated using different model descriptions, we will introduce two approximations which are used to explain several important concepts and definitions.

The Landau Distribution: For fast[3] charged particles with mass $m > m_e$ traversing thin layers of matter the straggling function is a LANDAU distribution $f_L\left(\Delta, x\right)$ which is given by

$$f_L\left(\Delta, x\right) = \frac{1}{\xi}\varphi\left(\lambda\right) \,, \tag{1}$$

[3] I. e. $\beta\gamma >> 1$.

where ξ is a proportionality factor given by references [7, 8] and $\varphi(\lambda)$ is a universal function of a single non-dimensional variable λ which is given by

$$\varphi(\lambda) = \frac{1}{2\pi i} \int_{\zeta - i\infty}^{\zeta + i\infty} \exp(u \ln u + \lambda u)\, \mathrm{d}u\,, \tag{2}$$

where ζ is any positive real number.[4] This universal function is a positive probability density function which has been normalised to an area equal to unity. The relation given by equation (1) scales and shifts the base distribution of equation (2). An example of a resulting LANDAU distribution is shown in figure 1. The LANDAU distribution exhibits an asymmetric

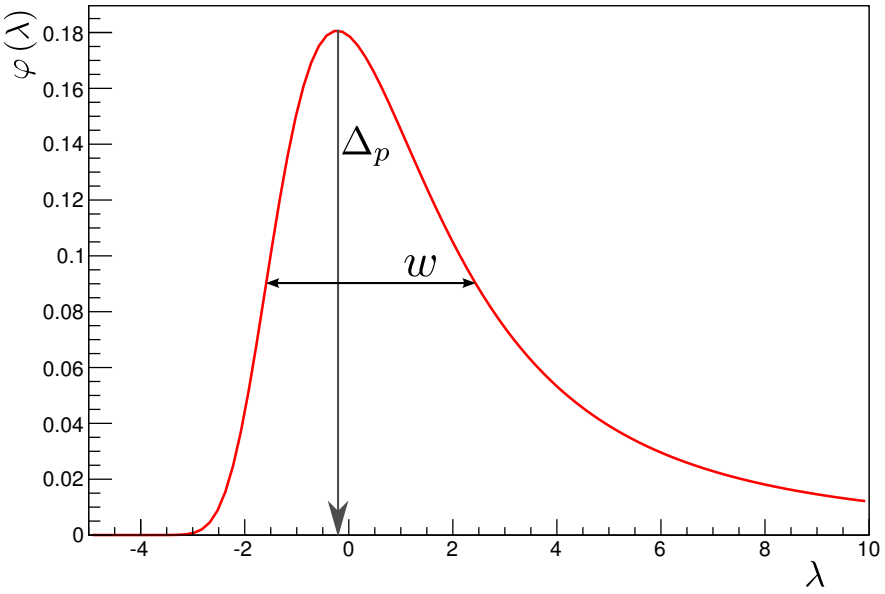

Figure 1.: LANDAU distribution with MPV at $\Delta_p \approx -0.222$ and width (FWHM) $w = 4$; calculated using the ROOT toolkit [9].

shape with a distinct peak and a very long tail. Due to the highly asymmetric shape and the long tail of the distribution it is not possible to define a mean or a variance, the statistical properties are given by the Most Probable Value (MPV) – which roughly coincides with the distribution's maximum – and the width w (this is the Full Width At Half Maximum or FWHM) [4]. Values larger than the maximum are favoured over values smaller than the MPV.

LANDAU derived his formula by using the RUTHERFORD cross section i. e. he assumes that the impinging particle is scattered on virtually free shell electrons.

The calculations which lead to the LANDAU distribution do not include factors related to the atomic structure [4]; LANDAU's approximation is merely an approximation of the actual straggling function. A more accurate calculation has been done by BICHSEL and is explained in [4].

[4] One can find that $\lambda \propto \frac{\Delta}{\xi}$ and $\xi \propto x$; see [7, 8] for full discussion and formulae.

The Bethe-Bloch Equation: BETHE [10] has calculated an approximation formula for the mean energy loss per unit length using the relativistic RUTHERFORD cross section and BORN's approximation. BETHE's calculation has been improved several times, the relation as is canon today [5] exhibits the proportionality

$$-\left\langle \frac{\mathrm{d}E}{\mathrm{d}x} \right\rangle \propto z^2 \frac{Z}{A} \frac{1}{\beta^2} \left[\frac{1}{2} \ln \frac{2m_e c^2 \beta^2 \gamma^2 T_{\max}}{I^2} - \beta^2 - \frac{\delta(\beta\gamma)}{2} \right], \tag{3}$$

where m_e is the electron mass, Z and A are atomic number and mass of the matter's atoms, z equals the projectile's charge, $T_{\max}$ is the maximum kinetic energy transferred to a free electron in a single interaction, I is the mean excitation potential of the material and $\delta(\beta\gamma)$ is a correction factor for the *density effect* (see [5]).

The BETHE-BLOCH equation is an approximation of the straggling function for thick segments of matter (i. e. a large number of individual scattering processes). When calculating the LANDAU theory for thick absorbers its shape becomes a GAUSSian distribution and matches the shape of the distribution defined by the BETHE-BLOCH formula. Like the LANDAU theory BETHE's formula can only be used to describe the behaviour of heavy particles ($m > m_e$). BETHE's relation holds only for $0.1 \lesssim \beta\gamma \lesssim 1000$ and an incident particle whose mass is larger than the electron mass m_e. The detector used in this analysis is 450 µm thick and thus the second criterion of the BETHE-BLOCH equation is violated.

It is to note that although the BETHE-BLOCH equation yields a quantity which is easy to interpret and calculate, the quantities that are more appropriate in a detector physics experiment are the MPV and width of the elementary straggling function.

Figure 2 shows the mean energy loss of a muon in copper, the validity region of the BETHE-BLOCH relation is shown in the central region. One can identify two different segments of the function in the BETHE-BLOCH approximation: For values lower than the minimum ionisation the mean energy loss is proportional to $\frac{1}{\beta^2}$, after the minimum it rises with proportionality to $\ln(\beta\gamma)$.

Minimum Ionising Particle: The point of minimum ionisation in the range of the BETHE-BLOCH (at $\beta\gamma \approx 3$) is used to define the concept of **minimum ionising particle** (MIP) i. e. a particle which exhibits the minimal possible mean ionisation energy $\left\langle \frac{\mathrm{d}E}{\mathrm{d}x} \right\rangle$ (cf. figure 2). Due to the fact that (on average) no particle deposits less energy than the MIP it is used to define a lower limit on detector requirements as any detector that can detect a MIP can (in principle) detect all particles of different energy as well.

The Bragg Peak: For a particle with $\beta\gamma < 3$ the mean energy loss $\left\langle \frac{\mathrm{d}E}{\mathrm{d}x} \right\rangle$ quickly raises with decreasing $\beta\gamma$ i. e. speed or momentum (cf. figure 2). With each segment of the trajectory

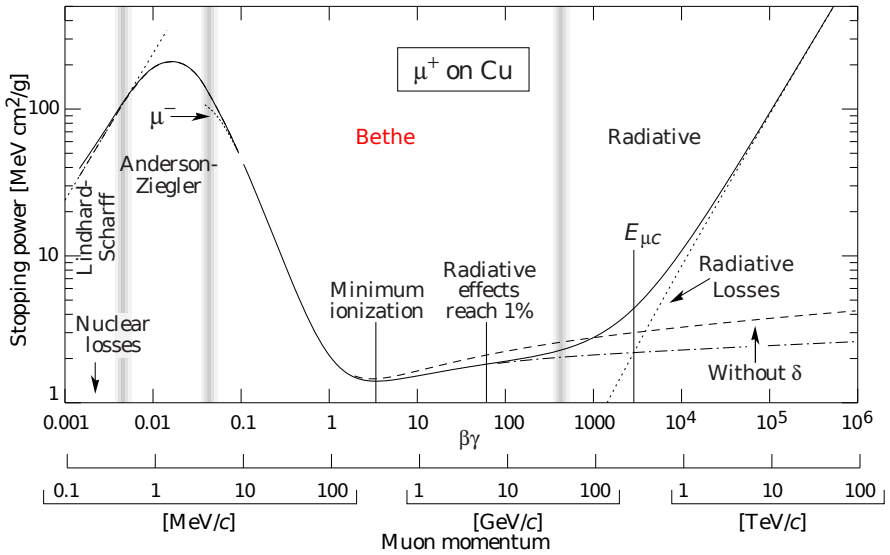

Figure 2.: Mean energy loss of a muon in copper as function of $\beta\gamma$, vertical lines indicate boundaries between different approximations. Region of validity of BETHE-BLOCH is marked with red text. Further explanation can be found in the origin of the diagram, see [5].

this effect increases as the particle has lost energy and thus the mean energy loss increases. As a result the particle is quickly stopped with a large energy deposition in the vicinity of the point of eventual rest. BETHE's formula – with some extensions – is able to describe this behaviour.

2.1.3. Urban Model for Ionisation And Excitation

The physical process of excitation is an electromagnetic interaction between a charged particle and an atom. In the event of a collision a certain amount of energy and momentum is transferred from the particle to a shell electron. In terms of elementary physical interactions the two interaction partners exchange a photon carrying the transferred momentum and energy. Having an energy above the ground state the electron changes into an excited state.
If the energy transferred exceeds the threshold of ionisation the shell electron is ejected from its atom and traverses the matter with kinetic energy $E = E_\gamma - W$, where E_γ is the energy transferred and W is the amount of energy necessary for ionisation. This ejected electron is called **delta electron**, its properties will be discussed further in section 2.4.

A very simple yet surprisingly accurate model for calculation of the energy deposition of a particle traversing matter is the URBAN model [11, 12]. The URBAN model assumes that the matter's atoms have only two energy levels with binding energies E_1 and E_2. This simplifies the particle's energy loss by excitation to a loss of either E_1 or E_2. Furthermore it is assumed that the energy loss due to the physical process of ionisation is distributed according to a function $g(E)$ with $g(E) \propto \frac{1}{E^2}$.

These simplifications allow a straightforward calculation of possible energy losses, however, it is necessary to calculate the macroscopic cross sections Σ_i for for the different interactions first; Σ_1 and Σ_2 are the cross sections for an excitation to the energy levels E_1 and E_2 respectively, Σ_3 is the cross section for the process of ionisation. The macroscopic cross sections derived in the URBAN model are listed in [12].
The number of excitation and ionisation processes occurring is sampled from a POISSON distribution, these numbers are then used to sample the corresponding energy loss contributions. For practical reasons the simple method explained above is extended by several special case conditions, some of which are explained in [11, 12].
The mean energy loss in a step can be calculated by summation of the contributing components and integration of the energy loss function $g(E)$ of the ionisation term (cf. ref. [12]).
Prior to simulation using the URBAN model its parameters have to be determined. This can be achieved by fitting experimental data and URBAN model with undetermined parameters. The fine tuning of the model parameters – as is the case for all simulation models – poses a task of great importance for any analysis performed with the data. As the URBAN model is the approximation of choice for electromagnetic interactions in simulations of high energy physics experiments we have chosen to use it for the calculation of the simulated data.

2.1.4. Ionisation Yield

The ionisation yield (i. e. number of secondary particles) of a particle passing the detector (i. e. primary particle) can be estimated in a simple model by assuming that an energy deposition of ΔE in matter creates

$$n = \frac{\Delta E}{W} \tag{4}$$

charge pairs,[5] where W is a proportionality factor. It has been shown that the actual proportionality factor W is larger than the band gap energy E_{Gap} due to several individual factors such as energy dissipation in the form of phonons [6, 13].
The proportionality factor $W = 3.6\,\text{eV}$ for silicon is approximately twice the band gap energy of $1.12\,\text{eV}$ [13]. It is to note that the model of the ionisation yield is independent of the model used to describe and calculate the ionisation processes.

[5] In silicon a charge pair is a pair of one electron and one hole.

2.2. Nuclear Event

A very rare process occurring in detector physics is the so called **nuclear event** [14, 15]. This is a hadronic process which results in the production of numerous secondary particles and the deposition of a very large amount of energy. Due to the fact that the resulting cluster exhibits similar properties as the cluster resulting from a delta electron event one must identify and exclude nuclear events from the data sample (they pose background for the analysis). Fortunately nuclear events are very rare and can be rejected easily by applying a cut which rejects clusters with a very large total signal. We have deployed an additional criterion for nuclear event rejection which is explained in section 6.2.

2.3. Multiple Scattering

A charged particle traversing matter is deflected by many subsequent scattering processes, which are COULOMB interactions between the particle's electrical field and the COULOMB potential of nuclei. The net result of these interactions is called **multiple scattering** (MSC). Figure 3 shows the different quantities that can be used to describe the process of multiple scattering, obviously MSC results in an angular deflection and a spatial reposition after passage of the absorber.

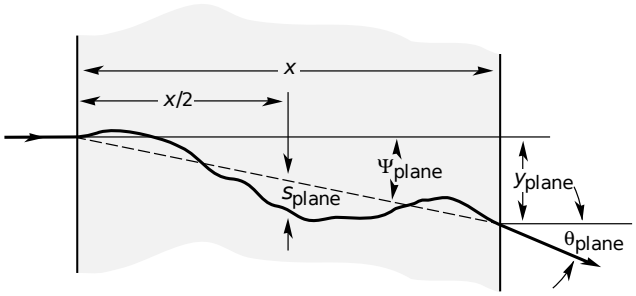

Figure 3.: Description of different quantities that describe the net effect of multiple scattering in a layer of matter; taken from [5].

For a thin detector one can usually neglect the lateral shift y_{plane} whereas the angular deflection θ_{plane} contributes even for very thin absorbers.
One can calculate the standard deviation of the planar scattering angle distribution of a particle passing through a block of matter with thickness $\frac{x}{X_0}$ (i. e. in units of the radiation length) to be

$$\sigma_\theta = \left\langle \sqrt{\theta^2} \right\rangle = \frac{13.6\,\text{MeV}}{pc\beta} z \sqrt{\frac{x}{X_0}} \cdot \left[1 + 0.038 \ln\left(\frac{x}{X_0} \right) \right] , \tag{5}$$

where p is the particle's momentum (in MeV/c), z its electric charge and $\beta = \frac{v}{c}$ its velocity in units of the speed of light [6].

2.4. Theory of Delta Electrons

A shell electron that is ejected from its atom due to ionisation by a particle is called **delta electron** or **knock-on electron**. Usually one denotes delta electrons which have sufficient energy to travel a measurable distance by the prefix "energetic" but this thesis discusses only energetic delta electrons, therefore we will abandon the prefix.
The path or trajectory a delta electron travels after creation is called **delta track** or **delta ray**. Obviously the distance a delta electron is capable of travelling is related to its momentum and therefore the momentum transferred from the original particle. While traversing matter the delta electron gradually deposits its energy, the amount over short distances x (in the order of the pitch of a pixel of the detector used in this thesis) is approximately given by a LANDAU distribution. When coming to rest the delta electron swiftly deposits an increasing amount of energy; the signal distribution along the delta track shows a BRAGG peak.
The relatively low energy of the delta electron results in severe angular deflection due to multiple scattering.[6] This influence of MSC makes the delta electron's trajectory very irregular (i. e. it's not similar to a straight line).
A pion of 120 GeV energy passing a silicon bulk of thickness 450 µm yields a deflection angle of $\sigma_{\phi,\pi} = 6.26\,\mu\text{rad}$; a delta electron with kinetic energy $T_\delta = 1\,\text{MeV}$ which passes through 1.5 mm of silicon yields $\sigma_{\phi,\delta} = 1.1\,\text{rad}$; the values used in these calculations are taken from the actual experimental data and a highly energetic delta electron event. The angular deflection of the delta electron is several orders of magnitude larger than that of the pion; although we can neglect MSC for high energy beam particles we cannot in case of delta electrons.
Figure 4 shows a schematic drawing of an event with a delta electron. The incident pion ionised the silicon bulk, in a small cylindrical area centred on its trajectory, when passing it. Among the low energy electron/hole pairs (which can be used to detect the pion) a single energetic delta electron was produced which travels along the trajectory t under the initial angle ϑ. Along this path electron/hole pairs are created which can be detected and used to reconstruct the delta electron's trajectory.
Under the assumption that the shell electron was resting previously to being ejected as a delta electron, the initial kinetic energy of the delta electron equals the transferred energy E_{loss} of the single ionisation process. As we have seen in section 2.1.3 this energy is selected randomly from the straggling function. The energy transfer E_{loss} yields a corresponding momentum transfer p_{loss} which *ipso facto* determines the ejection angle θ of the delta electron. As the two, E_{loss} and θ, are directly related we can assume that the ejection angle is stochastically

[6] Cf. equation (5): $\sigma_\phi \propto \frac{1}{\beta p}$.

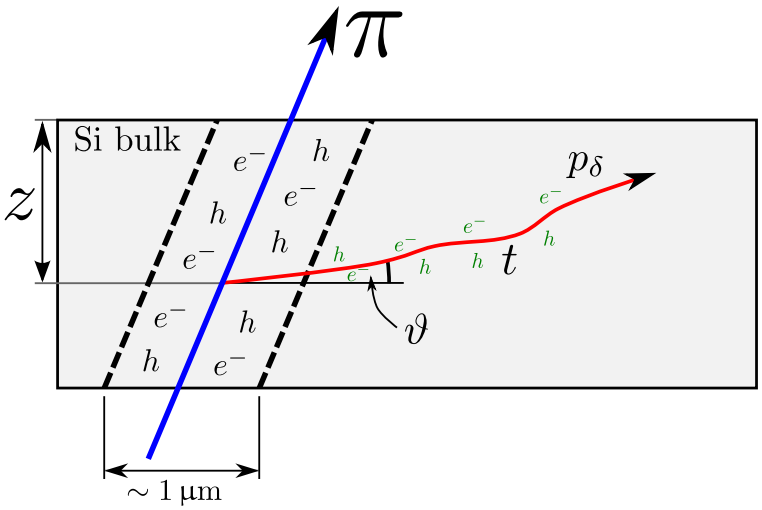

Figure 4.: Schematic drawing of delta electron created by a pion (blue trajectory) in a layer of silicon. Black e^-, h denote electron/hole pairs created by the pion, green ones are created by the delta electron whose trajectory is marked in red.

distributed by a distribution of similar shape as the straggling function.

We define the ejection angle θ to be the angle between the initial delta electron momentum and the incident particle's momentum prior to ejection of the delta electron. The angular distribution of delta electrons is given by [16]

$$\theta = \arctan\left(\frac{1}{\gamma}\sqrt{\frac{T_{\max}}{T} - 1}\right), \qquad (6)$$

where γ is the delta electron's LORENTZ-factor, T its kinetic energy and $T_{\max}$ the maximum energy transfer (see ref. [5]). This distribution yields angles very close to 90° for the relevant range of delta electron energies (cf. figure 5). The upper limit has been estimated by comparing the length of the longest delta electron trajectory[7] found in the analysis with the values in table 1.

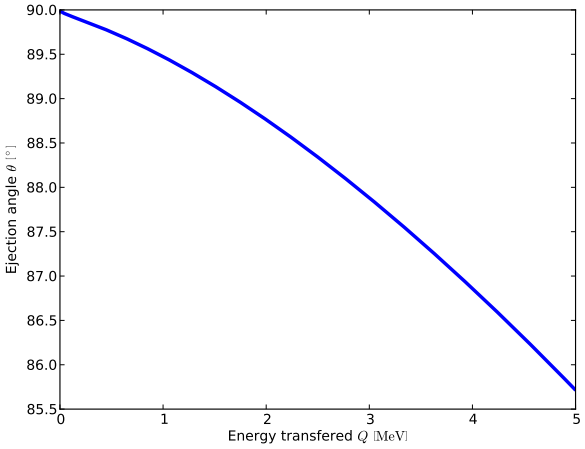

Figure 5.: Plot of the ejection angle θ versus the transferred energy Q for the relevant energy scale in this thesis.

The majority of delta electrons have a kinetic energy $T < 0.5\,\mathrm{MeV}$[8] and thus are ejected under an angle larger than 89.5°. This behaviour of the angular distribution is very fortunate for the analysis of delta trajectories in the detector plane: under the assumption that the pion beam hits the detector plane virtually perpendicular almost all delta electrons are ejected parallel to the detector plane and can thus be measured until their point of rest.

[7] Which was found to be 2.89 mm, unfortunately the values in table 1 end for $R = 1\,\mathrm{mm}$, thus we estimated the upper limit to be less than five times the value for $R = 1\,\mathrm{mm}$.

[8] Estimate from the trajectory length distribution found in the analysis.

One can approximate the number of delta electrons with energy $\geq E_\delta$ created per centimetre of the original particle's track by

$$\Sigma_\delta\left(E_\delta\right) \approx \underbrace{153\frac{\rho Z}{A}}_{:=y} \cdot \frac{1}{\beta^2 \cdot E_\delta\,(\mathrm{keV})} \left[\mathrm{cm}^{-1}\right] , \tag{7}$$

where ρ is the material's density (in $\mathrm{g}\cdot\mathrm{cm}^{-3}$), Z and A are its atomic number and mass and $\beta = \frac{v}{c}$ is the particle's speed in units of the velocity of light;[9] this approximation holds within a 10 % error [4]. While a particle traverses matter numerous delta electrons are created but only very few have enough energy to travel a measurable distance. This delta production fraction for different energies is one of the possible variables which shall be compared between the measured data and the MONTE-CARLO simulation.
The probability that a delta electron is created with enough energy to travel at least a distance of 50 µm is approximately[10] 8 % [13].

T [keV]	R [µm]	T [keV]	R [µm]	T [keV]	R [µm]	T [keV]	R [µm]
0.1	0.004	2	0.10	20	3.0	200	160
0.2	0.008	4	0.24	40	10	400	450
0.4	0.015	7	0.55	70	27	700	960
0.7	0.030	10	0.96	100	50	1000	1520
1	0.04						

Table 1.: Typical ranges R of electrons with kinetic energy T in silicon. For $T > 50\,\mathrm{keV}$ ranges were calculated using the algorithm given in [17]; for $10\,\mathrm{keV} < T < 50\,\mathrm{keV}$ ranges were calculated as in [17] and afterwards reduced smoothly to the experimental value at $10\,\mathrm{keV}$. Overall the uncertainty in R is estimated with 20 %. Taken from [4].

Due to the fact that delta electrons usually have low momentum the momentum reduction by large angle scattering has to be taken into consideration when estimating the effective range a delta electron may travel through matter. Table 1 shows estimated values of low energy electrons traversing silicon as calculated in [4].

[9] E_δ must be entered in keV; equation yields count per centimetre.
[10] Assuming an energy $E_\delta > 100\,\mathrm{keV}$ and a distance $x > 50$ µm in a block of silicon of thickness $d = 450$ µm.

2.5. The Truncated Mean Descriptor

Bichsel proposes a method of calculating the most probable value of the straggling function of a process by calculating the truncated mean; he defines the resulting variable C as the *truncated mean descriptor* [4]. The truncated mean is a measure of central tendency; it is calculated by discarding parts of a data set based on their deviation from the centre of the set.

Bichsel defines the descriptor C_j of the trajectory j for the cut percentage p (i. e. the percentage of entries that will be eliminated from the data set) by the relation

$$C_j^{(p)} := \frac{1}{n_t} \sum_{1}^{n_t} \frac{\Delta E_i}{x_i} ,$$

where n_t is the size of the truncated subset and $\frac{\Delta E_i}{x_i}$ is the signal deposited in the segment i weighted by the length of this segment. For practical purposes it is useful to require – independent of the percentage – at least a certain amount of entries to be removed from the set prior to calculating C (this is essential for small sets where $p \cdot n_{\text{orig}} < 1$). Usually it is assumed that the influence of x_i is either negligible or averaged [4] but can compensate large signals due to unusually long track segments. It is advised to use equidistant track segments.

To calculate the MPV of a straggling function it is practical to use the *one-sided* truncated mean i. e. the subset is defined by removing the largest n values.[11] This ensures that the rare low energy regime of the Landau distribution is sampled correctly and compensates for the long tail (cf. section 2.1 and fig. 1).

Which value to choose for p highly depends on the structure of the trajectories which shall be sampled; Bichsel recommends that the *truncation fraction*[12] $f_r := 1 - p$ may be between 0.5 and 0.7 [4].

The $C_j^{(p)}$ form a distribution whose maximal value defines the most probable value for the MPV of the straggling function. The moments M_i of the distribution of $C_j^{(p)}$ for $j \in J$ are defined as

$$M_1 := \left\langle C^{(p)} \right\rangle = \sum_{j=1}^{J} \frac{C_j^{(p)}}{J} \tag{8}$$

$$M_2 - M_1 := \sigma^2 = \sum_{j=1}^{J} \frac{{C_j^{(p)}}^2}{J} - \left\langle C^{(p)} \right\rangle^2 . \tag{9}$$

[11] Where n is defined as $n := \lceil p \cdot n_{\text{orig}} \rceil$.

[12] Defined for one-sided truncated mean.

2.5.1. Demonstration of Principle

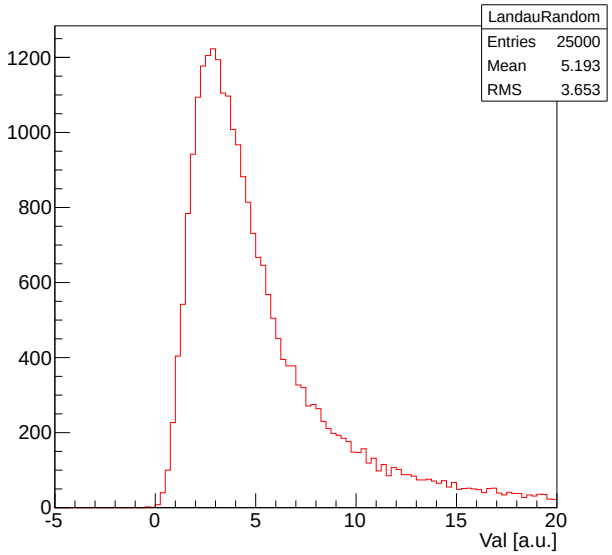

Figure 6.: LANDAU distribution with 25000 randomly selected entries. Distribution's MPV is at 3.0.

Figure 7 shows an example of an analysis using the truncated mean descriptor. For simplicity we choose a random number of entries per track (in the range $[3 : 30]$) and select a random value from the LANDAU distribution shown in figure 6 for each track segment. Surely this approach is over-simplified as not all track lengths are of equal probability (especially since tracks with more than ten steps are very rare). Afterwards each set of track values was analysed using different values for p, the results are shown in the example figure.

It is evident that the accuracy of the calculated MPV value depends on the value of p, due to the fact that higher values for p cut more entries of the low energy tail the resulting distribution has a maximum which is closer to the actual MPV.

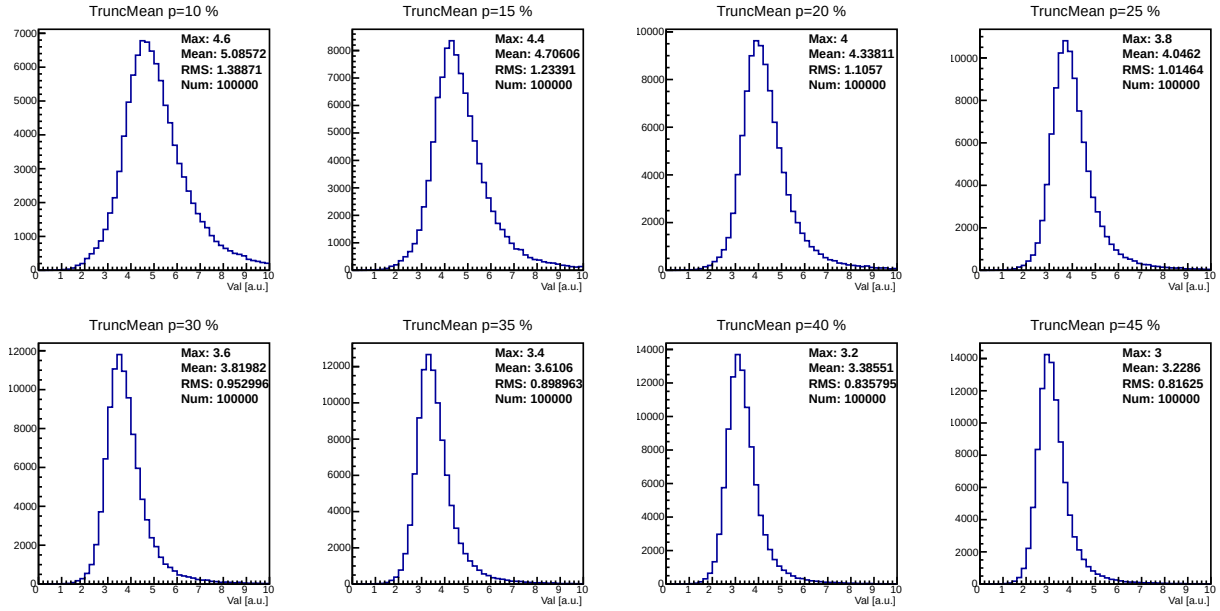

Figure 7.: Example analysis using the truncated mean method described in section 2.5 using values selected randomly from the LANDAU distribution shown in fig. 6 (has MPV at ≈ 3.0). Different plots show distributions of $C_j^{(p)}$ for changing values of p. Each individual track contained a random number (between 3 and 30) of entries of the LANDAU distribution; 100000 tracks have been randomly created and evaluated.

3. The DEPFET Detector

The ***De**leted **P**-channel **F**ield **E**ffect **T**ransistor* detector [18–20] is an active pixel detector. It has been successfully tested in several test applications [20–23] and its large scale application in the upcoming upgrade of the Belle II detector [19] is in preparation.

3.1. Operation Principle

The DEPFET pixel structure is obtained by combining a p-type MOS transistor with a fully depleted silicon bulk. The structure of one such DEPFET pixel unit is depicted in figure 8.

p-MOSFET: The *p-channel **M**etal **O**xide **S**emiconductor **F**ield-**E**ffect **T**ransistor* is a very common voltage-controlled transistor type. It consists of three contacts (source, gate and drain) which are created on an n-type substrate. The three contacts are placed next to each other with the gate contact in the middle. The source and drain contacts are p^+ doped and insulated from the gate contact by a thin oxide layer.
By applying a sufficient negative voltage to the gate contact (w. r. t. the source contact) an inversion layer is formed below the gate (in the substrate) and a channel is established between source and drain whose conductivity is controlled by the voltage applied to the gate contact.

Depleted Bulk: The unit's bulk is depleted using the technique of **sideward depletion** [22], that is to say the bulk is depleted by placing p^+ contacts on top and bottom, a shifted n^+ contact on the offside of an n-type wafer and applying appropriate voltages [18]. A potential minimum (for majority carriers i. e. for electrons in n-type Si) is formed where the two depletion zones (from top and bottom p^+ contacts) meet whose depth in the bulk can be controlled by the p^+ contact voltages. The potential is focused in a spatially restricted region by a deep n^- doping; this electrophile potential trap is called **internal gate**. For optimal operation it is necessary to place the internal gate in very close proximity to the MOSFET gate contact; in current applications it is approximately one micron below the surface [20].

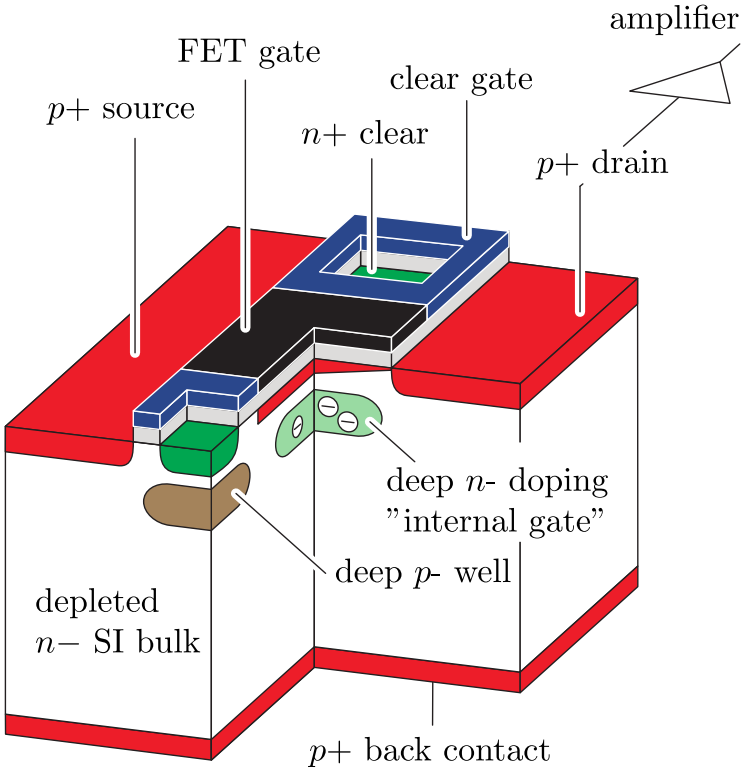

Figure 8.: Schematic drawing of a DEPFET pixel unit.

The Pixel Matrix Concept: For practical applications several hundreds of pixel units are combined in a matrix to a single detector module similar to the sensor of a digital camera. Within a detector module all units share the same source electrode which is kept at the same potential throughout all modes of operation.[13] Likewise the clear gate contacts of all units are connected and kept at a small negative voltage ($\sim 2\,\mathrm{V}$). The drain contacts of the units are connected column-wise and to a single Analogue-Digital Converter (ADC) per column. A very high negative voltage ($\sim -180\,\mathrm{V}$) is applied to the bulk contacts of all units and will be kept at that voltage during all modes of operation. The clear and the FET's gate contact are connected row-wise and the clear and gate contacts of each row are connected to a switcher contact which is shared per row.

Signal Collection: In the signal collection mode the FET gate contact is at a small positive voltage; the MOSFET is switched off. The clear voltage is placed at a voltage of approximately zero. A particle impinging on the Si bulk creates electron/hole pairs due to ionisation which are separated by the external field (resulting from the large bulk voltage); the holes flow to the backside contact and the electrons move towards the potential minimum where they will be collected in the internal gate. The clear gate potential serves as a potential barrier between internal gate and clear contact thus the electrons can be safely collected.

[13] Usually the source contact is used as voltage reference and thus it is defined that $V_{\mathrm{source}} = 0\,\mathrm{V}$.

Readout Mode: During readout a small negative voltage ($\sim -5\,\mathrm{V}$) is applied to the FET's gate contact which switches the FET into its "on" state. In this state a conducting connection is created between the source and drain contacts and due to the fact that both electrodes are kept at constant potentials a current flows through the FET. This current can be measured by the ADC connected to the drain contact.
The signal charges collected in the internal gate modulate the source drain current; the modulation is given by the equation

$$\mathrm{d}I_D = g_Q \mathrm{d}Q\,, \tag{10}$$

where $\mathrm{d}I_D$ is the current resulting from a collected charge $\mathrm{d}Q$ for a pixel unit with amplification g_Q [18]. During readout the signal charges remain in the internal gate therefore the measurement is non-destructive i. e. it can be performed several times on the same signal charges.
A more detailed explanation of the readout system used by the DEPFET detector can be found in [24].

Clear Mode: The signal charges are stored in the internal gate until a large positive voltage is applied to the clear contact which creates a highly electrophile potential and allows the signal charges to punch through the potential barrier of the internal gate towards the electrophile zone at the clear contact. A deep p-well has been implanted below the clear contact to rise a potential barrier between internal barrier and clear region which prevents charge loss during the collection mode.
After the internal gate has been cleared a second readout process can be used to measure the pedestal value. The pedestal value is the ADC value that is measured when there are no charges in the internal gate, it depends on differences between units due to fabrication and external conditions like temperature [13]. Due to the fact that it changes over time it must be measured or calculated regularly.
Even if a pixel has not been hit the clear process is necessary as it keeps the internal gate from saturating because the internal gate otherwise slowly fills with thermally generated electrons and other noise artefacts which shield the internal gate potential (resulting in an insensitive detector) [22, 25].

Gated Readout and Clearing: As stated before the pixels of a DEPFET module are arranged as a matrix and share several contacts row- and column-wise. Instead of using a dedicated readout and clear activation for each unit a switcher system is used to activate single rows for readout or clearing. The principle of this system is shown in figure 9.
The readout switcher activates all FET's of a single row, the currents flowing can then be

sampled by a single ADC per column. Afterwards the clear switcher pulses the clear contacts of all units in the very same row to clear the signal. Then the switchers move on to the next row and repeat the procedure.

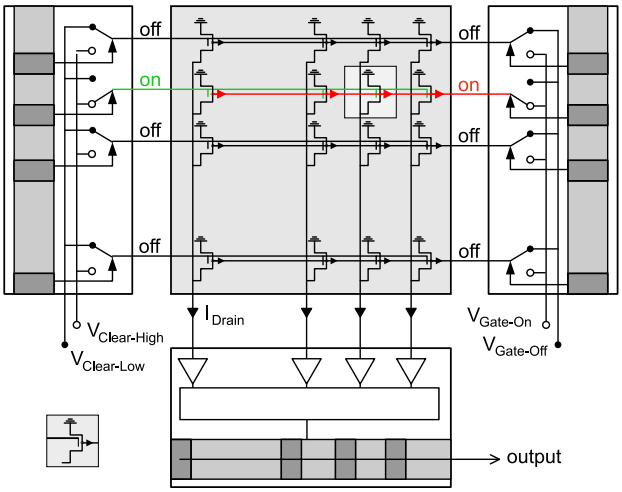

Figure 9.: Schematic drawing of the gated readout and signal purging method applied in the DEPFET detector. The clear and read switchers activate signal purging and readout row-wise (current row highlighted by coloured writing) while every readout channel (i. e. its ADC) reads the drain currents of the pixel in the same column. Figure taken from ref. [13].

This decreases the amount of ADC structures needed (and therefore reduces the material budget) while maintaining an acceptable readout speed. Additionally the gated readout system guarantees that there is no current flow in the non-activated DEPFET rows which ensures low power consumption of the DEPFET matrix [26].

The readout of the DEPFET is operated in the so called *rolling shutter mode*, that is to say that during charge collection phase the switcher continuously "scrolls" the DEPFET's rows and enables and disables the units of the current row. Once a trigger signal arrives the ADCs start taking data, i. e. data taking starts at a random row which is determined by the current "position" of the switcher chip. Unfortunately the data collected for the start row usually suffers from bad quality, a phenomenon called *start gate artifacts* (cf. [13]).

3.2. Specific Properties

Due to its intrinsic amplification stage and large depletion zone the DEPFET detector offers a very good Signal-To-Noise ratio (SNR) of 120 to 200 for pions of 120 GeV [21]. Its high SNR in combination with the DEPFET's small pixel pitch of 20 to 32 µm yields a very good intrinsic spatial resolution which is between 1 and 2 µm [21]. The large depletion zone and the intrinsic amplification stage allows to thin down the detector which in turn lowers the material budget, thus decreasing the effects of multiple scattering, which is one very important criterion for the DEPFET's use as vertex detector.

By using sidewards depletion the bias voltage necessary for full depletion can be up to four times lower in comparison with a p^+n diode [18].

Using modern semiconductor production technology it is possible to create the necessary structures for a DEPFET detector on an area as small as 20 µm, therefore yielding a very high pixel resolution.

By using the gated readout and clearing method the necessity for control structures can be reduced which decreases the financial cost and the material bill (→ less multiple scattering).

3.3. DEPFET and Delta Electrons

A quantity used for comparing the noise characteristics of semiconductor detectors is the Equivalent Noise Charge (ENC). The ENC is defined to be the amount of charges in the input node of a system (i. e. the number of signal charges in the internal gate of the DEPFET) in electrons that is equivalent to the total noise of the readout chain at the output node (usually given in ADC counts) [16]. A method for measuring the noise value is to place the detector in a pure environment (i. e. no particles are passing the detector) and calculate the fluctuation of the measured signal which should be distributed as a GAUSSian. The standard deviation of the GAUSSian can be used to estimate the noise value. Furthermore the ENC can be calculated from calibration constants like g_Q.
For the experimental setup used for collecting the data used in this thesis the ENC value was ENC $\approx 280\,e^-$. Due to the low noise profile of the actual detector stage the ENC is mainly influenced by the ADC and readout system and thus is highly dependent on the used setup. Generally the ENC of a readout system rises with increasing readout time.
The large depletion zone and the relatively thick modules used in the analysis ($d = 450\,\mu\text{m}$) provide a large sensitive volume. This is of great advantage for a delta electron analysis as the large depletion zone ensures highly accurate signals and due to the thick silicon bulk the probability of the creation of a delta electron is increased.
The good signal yield allows to resolve the small energies deposited by a delta electron (which are in the magnitude of few times of the noise value) and in combination with the very small pixel pitch, which is as low as $20\,\mu\text{m}$, even the trajectories of delta electrons can be resolved. The analyses that are undertaken in this thesis are only possible because of the very specific attributes of the DEPFET detector.

4. Test Beam

4.1. Experiment

The experimental data that was used in this thesis was taken during run *2169* of the test beam in 2009 at beam line *H6* of the CERN Super Proton Synchrotron (SPS).

Particle Beam: The particle beam used is created by colliding protons extracted from the SPS with a wolfram target. The secondary particles created in this collision – which are mostly pions – are processed (i. e. focused and channelled) for test beam usage.
The beam content used in the 2009 test beam session consisted of either electrons or pions at energies between 40 and 120 GeV. In run *2169* the beam consisted of pions at 120 GeV. The data sample of run *2169* is approximately 80 thousand events large.

Detector Setup: The setup consisted of six DEPFET detectors which were placed as close as possible to one another along the beam line to minimise the effects of multiple scattering (see fig. 10b for dimensions and arrangement). A particle hit was triggered using two scintillators in front and behind the six modules.

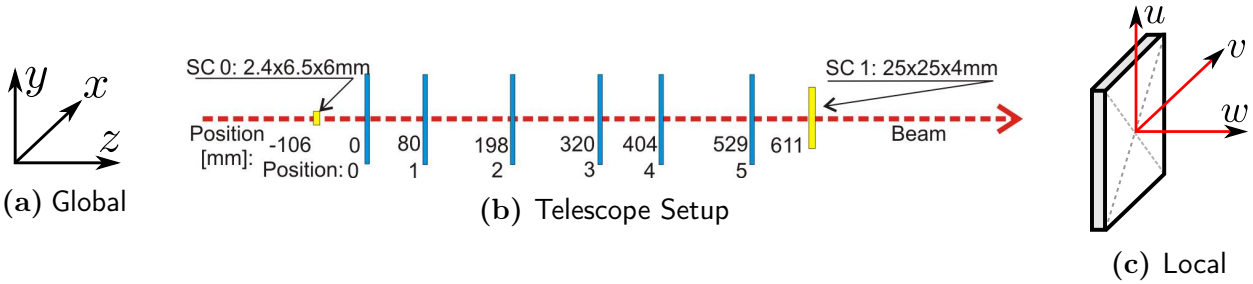

(a) Global

(b) Telescope Setup

(c) Local

Figure 10.: Telescope arrangement properties. Fig. 10a: Global (telescope) coordinates. Fig. 10b: Detector arrangement in the telescope along the beam line as used in the 2009 test beam, SC marks trigger scintillators, position along beam line is given in global coordinates; taken from [21]. Fig. 10c: Local (per detector) coordinates.

The telescope was comprised of five detector modules, which were of the same type; their parameters have been kept constant throughout the different runs and they were used as

reference modules. The sixth position (located at mounting point two downstream from the first scintillator, counting starts at zero) was inhabited by three different modules on which the different tests were performed, the currently active was called Device Under Test (DUT). The telescope setup allows to reconstruct the event data using five reference modules which have been well-studied in previous experiments. Later this reconstructed data can be compared to the data gathered from the DUT and its performance can be analysed.

Coordinate Systems: The global coordinate system depicted in figures 10a and 10b corresponds to the lab coordinate system, it is a Cartesian coordinate system where z equals the beam axis. The local coordinate system is a per detector coordinate system whose origin is placed in the centre of the detector. It is a Cartesian coordinate system where w equals the normal vector of the detector module and u and v are in the detector plane. A rotation of the detector module is parametrised by the three EULER angles α, β and γ. One can transform a global coordinate $\vec{r} = (x, y, z)$ into a local coordinate $\vec{q} = (u, v, w)$ using the relation

$$\vec{q} = \mathcal{R}_i \left(\vec{r} - \vec{r}_0^{(i)} \right) ,$$

where $\mathcal{R}_i = \mathcal{R}_i \left(\alpha_i, \beta_i, \gamma_i \right)$ is the rotation matrix of module i and $\vec{r}_0^{(i)}$ its shift from the global coordinate origin.

Any event reconstruction needs full telescope data and therefore it is essential to perform an alignment of the telescope modules, i. e. to calculate the shift (coordinates u, v, w) and rotation (coordinates α, β, γ) of every telescope module.

Detector Modules: The detector thickness for all modules was 450 µm for pixel matrices of size 64×256 pixels.

For the delta electron analysis all telescope modules are treated equally because this analysis does not evaluate the performance of the single DUT but the performance of the MONTE-CARLO simulation in comparison with similar physical detectors. Table 2 lists the properties of the DUT modules used during the test beam; the DUT used during run *2169* was the **STD** module.

Using equation (5) one can calculate the expected angular opening due to MSC of a parallel 120 GeV pion beam interacting with a detector module of above dimensions to be approximately 6.26 µrad,[14] the resulting spatial reposition after passage of the whole test beam setup equals 1.7 µm which is in the order of the spatial resolution of a single module. However, due to the fact that the total reposition is comparably small we will neglect the effects of multiple scattering on the pions in the course of the analysis. The telescope modules have

[14] Using the silicon radiation length of $X_0 = 9.36\,\text{cm}$ [5].

DUT	S/N	$g_Q\ \left[\frac{\text{nA}}{e^-}\right]$	$\Delta A\ [\text{mm}^2]$	dir.	$P\ [\mu\text{m}]$	$\Delta d\ [\mu\text{m}]$
STD	128.4 ± 2.8	379 ± 15	1.536×6.144	x	24	1.19 ± 0.16
				y	24	1.39 ± 0.06
C3G	148.4 ± 5.2	516 ± 21	2.048×6.144	x	32	1.55 ± 0.13
				y	24	1.51 ± 0.06
HiG	213.3 ± 7.7	688 ± 27	1.280×5.120	x	20	1.03 ± 0.19
				y	20	1.34 ± 0.07

Table 2.: Properties of the DUT modules used in the 2009 test beam: **S/N**: Signal-to-noise ratio; in-pixel gain $\mathbf{g_Q}$; active area size $\mathbf{\Delta A}$; pixel pitch $\mathbf{P}$ and spatial resolution $\mathbf{\Delta d}$ per direction. Taken from [13].

similar properties as the STD module except for their pixel pitch which is $32 \times 24\,\mu\text{m}$.[15] Further information about the test beam at CERN SPS and its results can be found in the paper of the associated analysis [21].

4.2. The Test Beam Reconstruction Chain

Prior to any analysis it is necessary to reconstruct the actual particle hits and their corresponding particle tracks from the raw detector data. In order to do this several processors for the `ILCSoft` analysis framework [27] have been – specifically for the DEPFET analysis chain – developed.
In this section these processors shall be presented and their purpose will be explained in detail. The flow of the reconstruction chain and the successive delta ray reconstruction and analysis is depicted in figure 11. The parameters used by the reconstruction programs are listed in appendix A.

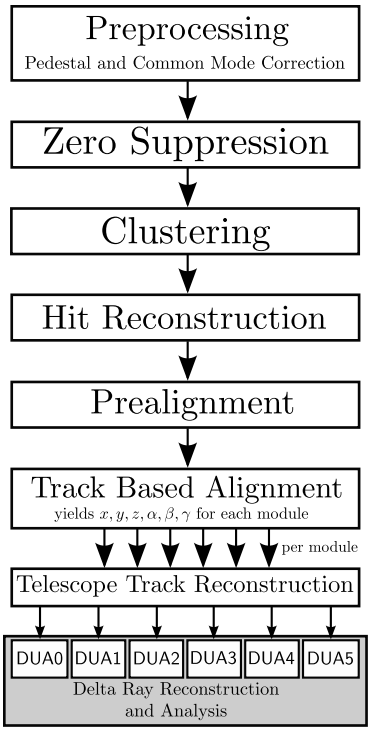

Figure 11.: Diagram of analysis flow, grey box depicts delta ray analysis.

4.2.1. Pedestal and Common Mode Correction

The raw signal of pixel i, j measured by the test beam setup is composed of four different contributions [13]: the pedestal value, the common mode noise, the GAUSSian readout noise and the charge signal:

$$S_{ij}^{\text{raw}} = S_{ij}^{\text{ped}} + S_{ij}^{\text{cm}} + S_{ij}^{\text{noise}} + S_{ij}^{\text{sig}}\,.$$

[15] Naturally this changes the active area, which is defined for direction i by $\Delta A_i := P_i \cdot N_i$ where P_i is the pixel pitch and N_i is the number of pixels in the matrix in direction i.

Two contributions, the pedestal value and the common mode noise can be entangled in the preprocessing. The pedestal value – sometimes called dark pixel value – is the base pixel value that is measured when no charges are collected. It can either be measured (cf. section 3.1) or calculated from the raw data using frames without hits.
The common mode arises from the fact that the gated readout technique on the double pixel (i. e. two pixel share a source contact) of a DEPFET module induces a noise component. This noise is row-wise correlated [13] and in the order of ≈ 20 adu. It can be calculated from the raw data measured during the test beam.
The corrections for pedestal and common mode have been done previously by Geisler [13] and are explained there in great detail.

4.2.2. Zero Suppression

The DEPFET Detector yields full-frame data in a matrix format, that is to say the data file includes the pixel information of all pixels for each event. Fortunately, however, the majority of the detector will only contain noise as a particle hit is usually limited to very few pixel and the number of hits in a test beam setup is very low.
The zero suppression processor takes the raw data collection, the detector's status map and the corresponding noise map and returns a collection which contains only pixel with good status and whose signal value exceeds the noise value by a certain factor.

4.2.3. Clustering

In order to identify particle hits and perform an analysis on the signal distributions on the detector it is crucial to have an efficient and effective clustering algorithm. This clustering algorithm joins adjacent firing pixels to a new object called cluster which – in theory – should eventually contain all signal generated by one hit.
Using the zero suppressed data the processor searches possible cluster candidates by combining pixel which are nearest neighbours. The criterion of the nearest neighbour can be applied with different levels of strictness, the most strict allowing only merging of pixels with common edge and the most lenient allowing merging for pixel which are separated by a one-pixel gap. After all pixels have been merged to cluster candidates it is checked whether the clusters comply with different signal criteria.

4.2.4. Hit Reconstruction

The next step is to identify particle hits from the cluster data which was yielded by the previous processor.
A sophisticated approach for track reconstruction is to apply a centre of gravity (COG) algorithm, which weights the pixel signal's and their position; the hit position r is then given by

$$r = \frac{1}{\sum S_{ij}} \sum r_{ij} S_{ij}$$

with S_{ij} being the signal at the pixel centre r_{ij} (in local coordinates). Figure 12 shows a schematic drawing of a hit cluster and the reconstructed hit position. In general this algorithm performs well and is very robust therefore it is used in the reconstruction chain for this thesis.

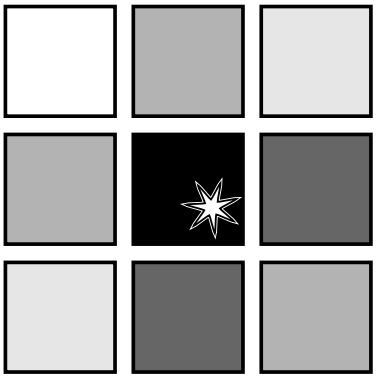

Figure 12.: Schematic representation of centre of gravity position finding algorithm, depicted are nine pixels with measured signal (light → low signal, dark → high signal) and the resulting reconstructed hit (marked by star) [13].

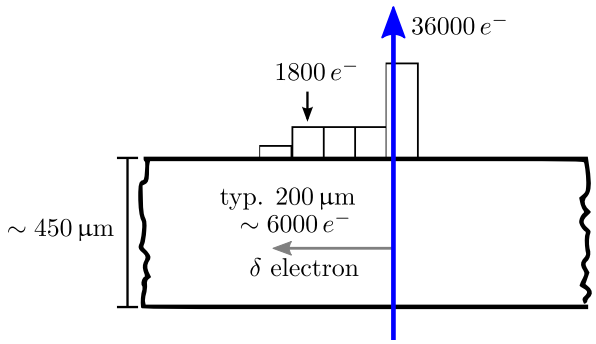

Figure 13.: Effect of signal deposited by delta electron on the hit enlargement; values are estimated from actual analysis results of the test beam data i. e. for a pion of 120 GeV impinging of 450 µm silicon. The typical delta event is taken as most probable delta event found in the analysis (cf. section 7.2).

The hits calculated here will only be used for the reconstruction chain because neither of the hit making algorithms implemented in the processors of the reconstruction chain can cope with the peculiar geometry of delta clusters. Figure 13 shows the enlargement of the cluster of a hit with a delta electron. Obviously a pure COG hit reconstruction algorithm will place the hit falsely for the example depicted, it suffers from a systematic uncertainty. This can be solved by removing the delta trajectory segment from the cluster prior to the hit reconstruction. The results of this thesis may be of help when developing a routine that is capable of doing this.

4.2.5. Prealignment

The correlator processor performs a prealignment of the different telescope detector modules in the $x - y$-plane, the plane perpendicular to the particle beam.
This is done under the assumption that the particle beam is along the z-axis and has a very low spread ($\rightarrow$ small opening angle). This allows only one free parameter for any full-telescope particle track: the hit position on a reference plane. Using the hit on the reference plane hits on the other planes are matched and the deviation of these hits from the straight line fit is then used as alignment correction. The actual alignment correction is determined by selecting the most-probable value from the histogram of all alignment corrections in the analysis data sample.
This method is insensitive to misalignment in z-direction and its performance is affected by *a*) a beam that is not parallel to the z-axis *b*) rotated detector modules; or *c*) a beam with wide spread. After the prealignment a set of starting values of the three spatial coordinates and three rotation angles of every modules is known. The position of the modules along the beam line (i. e. z-axis) is taken from the measurements of the telescope, the x and y components is calculated by the prealignment and the three rotation angles are estimated to be zero (i. e. no rotation).

4.2.6. Alignment

The main alignment of the telescope modules is done using two different processors.
At first a set of telescope tracks is gathered which comply with a number of very strict criteria. This is done by matching all possible hit patterns using a Combinatorial Kalman Filter (CKF) to gather track properties and finally selecting the optimal set of tracks from these properties. The selection is based on the track χ^2 (which is to be minimised); the optimal selection guarantees that no hit is assigned to two tracks. As the tracks will be used for alignment purposes only we demand that each of the reconstructed tracks hits all telescope modules.
The second step is to use these alignment tracks with a Kalman filter for alignment [28–30], this is done by calculating the evolution over the course of the run for each alignment parameter from the alignment tracks. Eventually this data set allows the alignment of the telescope modules in both tilt and shift with a very high precision of $< 0.1\,\mu\text{m}$ for shifts and $< 10^{-5}\,\text{rad}$ for tilts.

4.2.7. Track Reconstruction

The track reconstruction uses the same data processor that has already been used for the main alignment and has already been described in subsection 4.2.6. However, as this step should reconstruct tracks for analysis we use a changed set of thresholds for the steering variables.

5. Monte-Carlo

The MONTE-CARLO simulated data that was used in this thesis was calculated using the `Mokka` toolkit [31] with `Geant4` [11, 12, 32] in version *4.9.3.p01* as physics simulation and a DEPFET digitiser simulation [33].

5.1. Simulation Characteristics

The simulation of a particle passing through a detector plane is split in two steps [13]: first the physics processor `Geant4` simulates the interaction of the incident particle with the sensor bulk. This process is controlled and executed by the `Mokka` package; within this wrapper the individual beam particles are tracked through all layers of the telescope.[16] The trajectory and passage simulation is split in *G4-steps*, that is to say track segments for which the physical quantities (e. g. energy loss, angular deviation etc.) are calculated and stored explicitly.
Afterwards the digitiser stage uses the combined set of all `G4-steps` to simulate the charge collection (i. e. the actual detector) [13, 33]. This is done in three separate steps: 1st: The energy loss between two segments is converted into the number of created signal electrons. These signal charges are grouped in clusters called *ionisation-points* and placed along the track between the two segments. 2nd: Now the electron drift and diffusion in the detector bulk is simulated. The digitiser stage uses simplified model assumptions of the DEPFET's electric field distribution. A GAUSSian noise is added which reflects both amplification and sampling noise. Afterwards the zero suppression is applied and the data of the remaining firing pixels is stored.
Figure 14 shows a schematic representation of the digitiser simulation. The performance of the digitiser stage is discussed in reference [13] extensively.
The physics list used in the simulation by `Geant4` was the `QGSP_BERT`[17] list. This physics list is the one currently most recommended for high energy physics experiments by the `Geant4` developers [32]; possible models mostly differ in the simulation of the hadronic interactions which are of little interest throughout this thesis. The more relevant electromagnetic inter-

[16] Those layers are silicon (sensors), air and other materials (e. g. support structure).
[17] `QGSP` is an abbreviation for **Quark-Gluon String Precompound**, `BERT` for **BERTINI Cascade Model**.

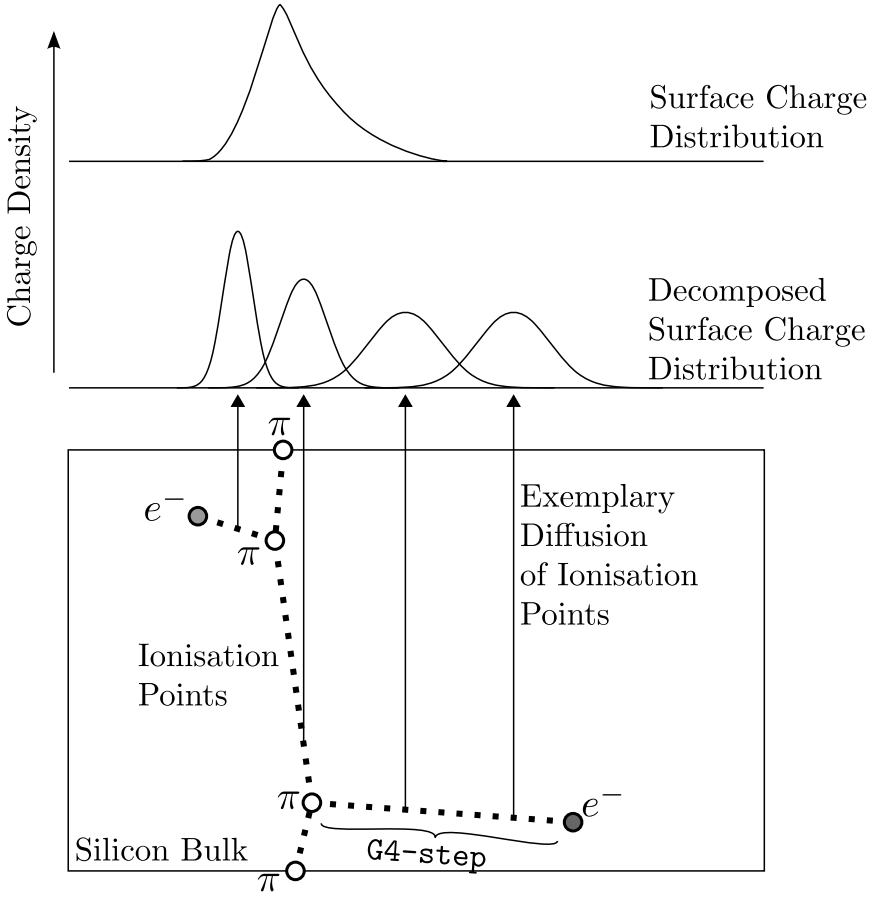

Figure 14.: Scheme of operation of digitiser stage simulation. A pion's trajectory through the silicon bulk is sampled in `G4-steps` (steps between white filled circles), delta electrons created are sampled similarly (grey filled circles). The total energy loss per `G4-step` is distributed in *ionisation-points* along the segments. The ionisation-points may be smeared due to diffusion while drifting towards the sensor surface (lateral diffusion is dependent on diffusion length). The surface charge distribution is composed of the contributions of the individual ionisation-points' charge distribution; the decomposed surface distribution is integrated and a GAUSSian noise component is added. Modified version image taken from [13].

actions are usually simulated by the **Standard EM Model** which uses the URBAN model – which has been explained in section 2.1.3 – for simulation.

`Geant4` allows the generation of a delta electron only if the transferred energy exceeds a threshold energy T_c, whose value is defined by atomic parameters and a material specific cut value T_{cut} [11]. Below the threshold specified by T_{cut} the soft secondary particles are simulated as continuous energy loss of the original particle, above the ejected delta electron is simulated explicitly.

The value used for T_{cut} is actually given as threshold range r which is then converted – by `Geant4` – to a corresponding range. We used a range cut of $r = 1$ µm in silicon.

5.2. Detector Calibration

Due to the fact that the test beam (TB) data is gathered in a real life setup, including a full readout chain, the signal values stored in the data files are given in ADC counts (ADC units, ADU). The MONTE-CARLO (MC) simulation on the other hand is performed without a readout chain and thus without an ADC; the signal values are given as the actual number of electrons N_e created by ionisation and collected in the internal gate.
In principle one can convert the number of electrons to the resulting drain current using equation (10), afterwards the actual ADC value is given by the ADC's range and conversion factor; the two steps can be executed in one by combining the conversion factor and g_Q. Unfortunately the conversion factor is not known *a priori* and must be extracted from the test beam data. For simplicity we assume that all charges created by ionisation are collected in the internal gate by diffusion or drift i. e. we assume no charge losses. Due to the fact that each DEPFET module has its own ADC the conversion factors differ slightly between modules. As a rule of thumb: 15 ADU approximate to 280 e^-.
The actual conversion factor k, defined via the relation

$$1\,\mathrm{ADU} \equiv k \cdot N_e$$

can be calculated for a defined pair of MONTE-CARLO and test beam data by fitting the cluster charge distributions of MC and TB on a per detector basis using one parameter which is multiplied to one of the data sets (the basic principle is similar to the method described by BICHSEL in [4]). In this analysis we chose to measure all charges in ADU therefore we matched the cluster charge distribution of each TB module to k times the charge distribution of the MC module with the same plane number.

Plane No.	0	1	2	3	4	5
Conversion factor k [adu]	0.0535	0.053	0.0477	0.0505	0.05	0.051

Table 3.: Conversion factors from N_e to ADU for used MONTE-CARLO data in reference to test beam data.

This yields the conversion factors listed in table 3, the (logarithmic) plots of the charge distributions of the different modules for the test beam data and the MC data have been included in figure 16. They show very good agreement of the peak and the upper flanks for all modules except module *0*. After realising that full matching of the distributions is not possible for module *0* we chose to match the peak position as well as possible, however, this impairs the matching of both flanks.
The TB data shows a very distinct low signal tail which can be explained by the start gate artifacts explained in section 3.1; these artifacts can be removed from the data sample, however, we refrained from doing so as we assume that this is not of importance for the delta

ray analysis. The large fluctuations of the distributions for large signals can be explained due to bad choice of binning. The binning depicted was chosen because it allows to match the peak and the upper halves of the flanks with high precision, unfortunately this degrades the quality of the plot in the region of high signals.

5.3. Data Cross-Check

Prior to analysing the properties of delta electrons in the different data samples we performed a cross-check of the data sample. Under the assumption that the MC sample yields physically correct events the distributions of quantities like the cluster size should be very similar when comparing the two data sets.

Thus we performed an analysis of the cluster size distributions on a per module basis regardless of the individual event's delta classification (i. e. the whole data sample was used).
We find the distributions for the different modules of the two data samples to be in very good agreement, figure 15 shows these distributions for two exemplary modules. Module *2* is the only used module with pixel pitch 24×32 µm which generally yields larger clusters (maximum of distribution in fig. 15a is shifted rightwards is comparison to fig. 15b). This is a direct result of a smaller pixel pitch as the physical charges are measured by more physical pixel units (the process of reading a common charge source with different pixel units is called charge sharing) which in turn yields more firing pixels per cluster i. e. a larger cluster size.
The effect is most prominent in the distribution of the cluster size projected to the column direction as this is the direction in which the pixel pitches differ.

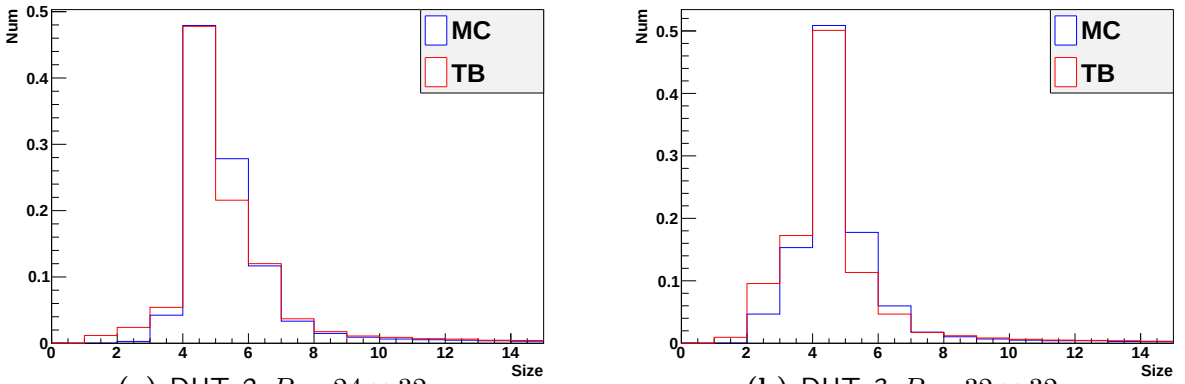

(a) DUT *2*, $P = 24 \times 32$ µm **(b)** DUT *3*, $P = 32 \times 32$ µm

Figure 15.: Cluster size distributions for experimental and Monte-Carlo data sample for modules *2* and *3*. Distributions have been normalised to an area equal to unity.

In conclusion we find very good agreement of the different distributions for the two data samples. This allows us to continue analysis and perform the actual delta electron reconstruction and analysis.

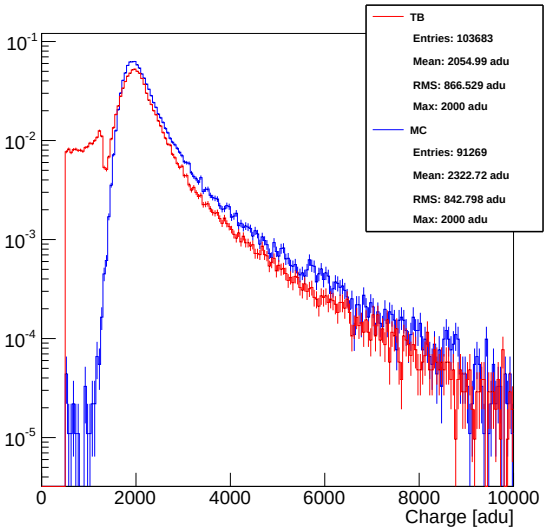

(a) Module *0*

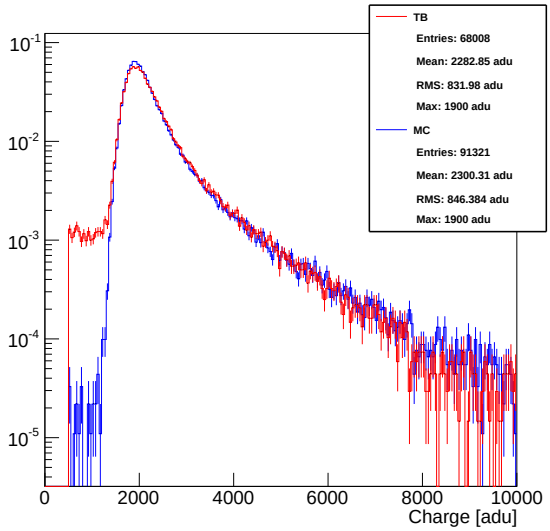

(b) Module *1*

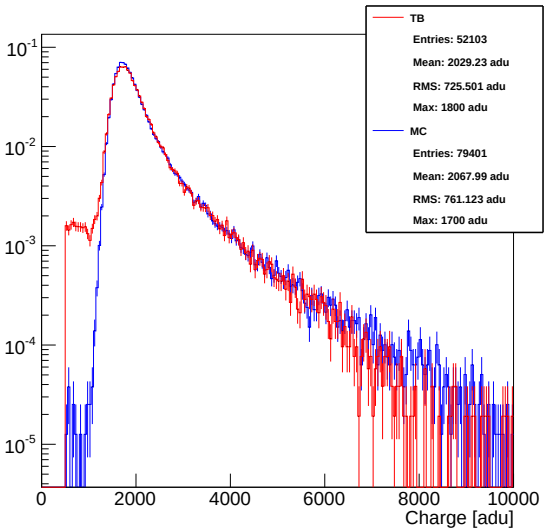

(c) Module *2*

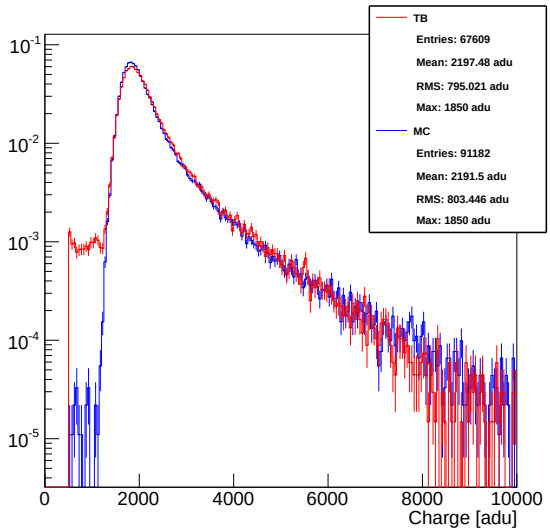

(d) Module *3*

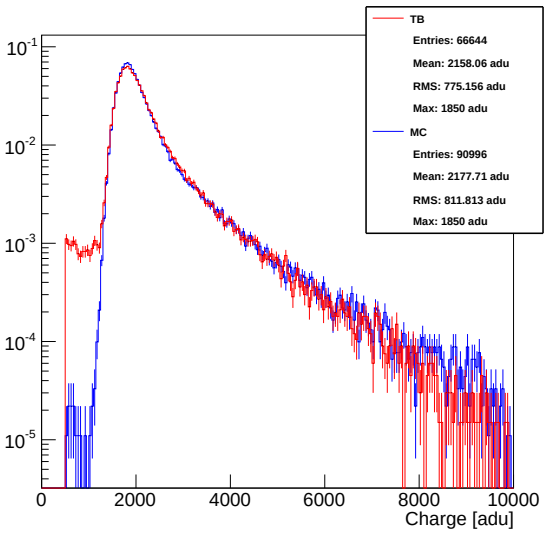

(e) Module *4*

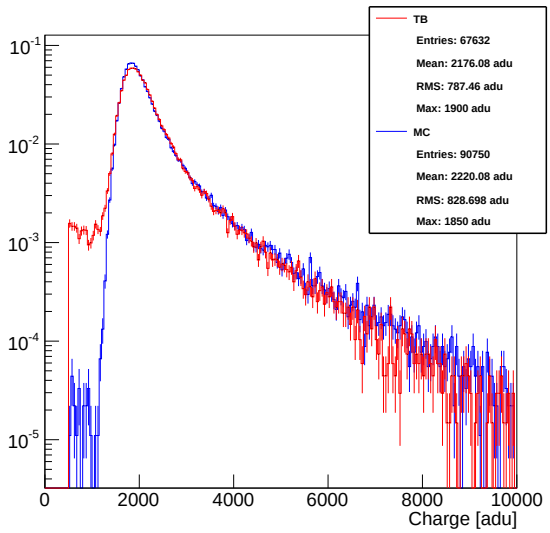

(f) Module *5*

Figure 16.: Charge calibration plots, conversion factor k already applied to MC data sample.

6. The Delta Ray Analysis Program

6.1. Analysis Concept

The goal of the delta ray analysis program is to select a set of delta clusters from the initial data sample and transform the abstract pixel matrix given by the previous reconstruction programs (cf. section 4.2) into an object which describes the characteristics of the individual delta events. Prior to explaining how to parametrise a delta cluster it is useful to discuss some of its characteristics.
It is to note that from here on the term "track" is to be understood as delta trajectory, the pion track through the whole telescope will be named *telescope track*.

6.1.1. Delta Cluster Characteristics

The physical depiction of a delta electron has been shown in figure 4; the measured signal can be seen as a pixel matrix of values, an example is shown in figure 17. Shown is a segment of the pixel matrix of the detector i. e. the pixel coordinates (in pixel ID) are shown on the two axes. The colouring of the individual pixel entries corresponds to their signal. Entries which are white depict blank pixels i. e. pixels without a signal.

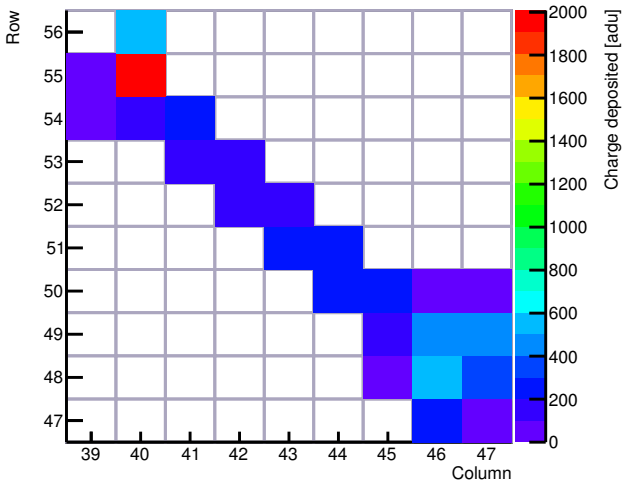

Figure 17.: Example of delta cluster with telescope track cluster and BRAGG cluster. Telescope track hit in upper left corner, BRAGG cluster in lower right corner.

A typical delta cluster is comprised of at least two different characteristic segments: Where the telescope track hit the active plane one can find an (more or less) ellipsoid cluster segment which is the result of the initial telescope track hit. It is usually contained in a rather small area, typically inside a 3×3 pixel area. The properties of this segment should in theory be very similar to ordinary

(non delta) clusters and can therefore be used to calibrate the signal. In figure 17 one can identify the telescope track hit cluster segment in the upper left corner.
Another segment every delta cluster is comprised of is the delta trajectory segment which is usually a rather thin segment that can stretch for several tens of pixels. This segment is the most important part of the cluster for a delta electron analysis as the whole energy deposited within this segment was carried by the delta electron and the scattering processes experienced by the delta electron define the curvature of the segment. The above example shows a rather thin delta trajectory cluster segment which expires in an optional cluster component: the BRAGG cluster segment.
In most cases when a delta electron comes to rest and deposits its remaining energy in a BRAGG peak (cf. section 2.1) the delta trajectory exhibits an (more of less) ellipsoid cluster segment at the end of the trajectory. This is a result of the fact that the large number of charges created by the halting delta electron in the detector's silicon bulk can diffuse and thus spread further while maintaining a significant (i. e. measurable) signal. Referring to the above example one has to note that the BRAGG cluster segment depicted is rather large, usually it can be contained in a 3×3 pixel area.
In case that the delta cluster is rather small (i. e. the delta trajectory is fairly short) the different segments blend into each other and cannot be separated easily.

Device Under Analysis (DUA): The DUA is the telescope module which is analysed in the current analysis step.
The special properties of a delta cluster cause great problems for the track finding algorithm due to bad hit matching (cf. section 4.2.4). It is, however, possible to manually fit the telescope track to a selected delta event by disallowing the track finding algorithm to match its tracks to the DUA and then – in the actual delta track processor – calculating the point of impact of the telescope track on the delta cluster. Therefore we deemed it necessary to split analysis starting from the track finding algorithm into a per-detector analysis. That is to say the delta ray reconstruction and analysis is performed on a per-module basis with the DUA being the module whose delta events are currently analysed.

6.1.2. The Delta Trajectory

For this analysis it is necessary to identify the trajectory of the delta electron, i. e. to transform the pixel matrix representation shown in figure 17 into the track representation shown in figure 18 (the black arrows depict the track steps).

This poses several problems: There may be multiple delta electrons created in one event and thus there may be multiple tracks originating from the telescope track hit or the delta tracks may branch.

Furthermore there may be gaps in the delta track as the charge deposited may be lower than the zero suppression threshold (due to the fluctuations in the charge deposition described in section 2.1). A still rather small in-track gap is depicted in figure 19a. The delta electron can change direction rapidly and severely, resulting in a heavily curled trajectory as shown in figure 19b. These two classes of problematic situations are especially tricky because to resolve these an algorithm must check a wider range of possible next track steps which may yield false results for delta clusters which are composed of extensive areas of firing pixels (a problematic situation as well).

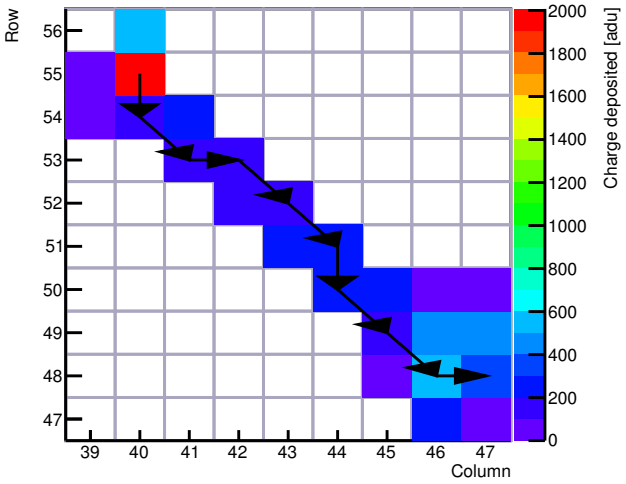

Figure 18.: Delta trajectory calculated from the cluster already given in fig. 17. The black arrows represent the delta trajectory i. e. the delta electron was created in the upper left corner and came to rest in the lower right corner.

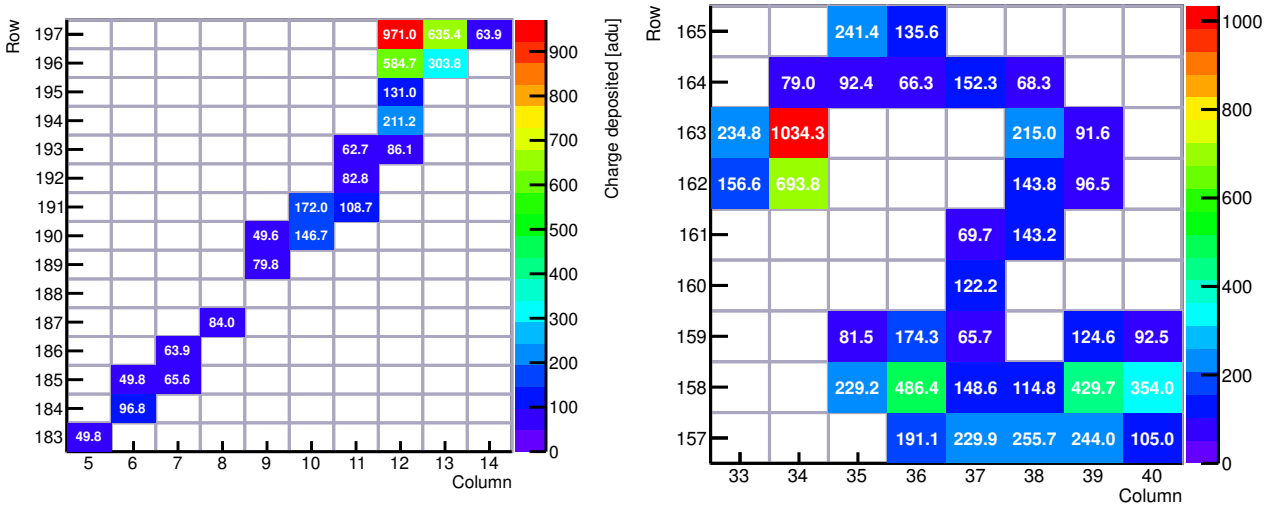

(a) Track Gap

(b) Heavily Curled Track

Figure 19.: Examples of problematic situations for a delta trajectory determination algorithm; white numbers show pixel signal value in adu.

To be able to use the full data sample and perform an analysis as unbiased as possible, it

is necessary to cope with these situations. Naturally no one algorithm can identify all delta events correctly and determine the exact delta trajectory in all cases, thus it is necessary to implement quality checks which reject single events based on the compatibility of the calculated delta characteristics with the pixel matrix.

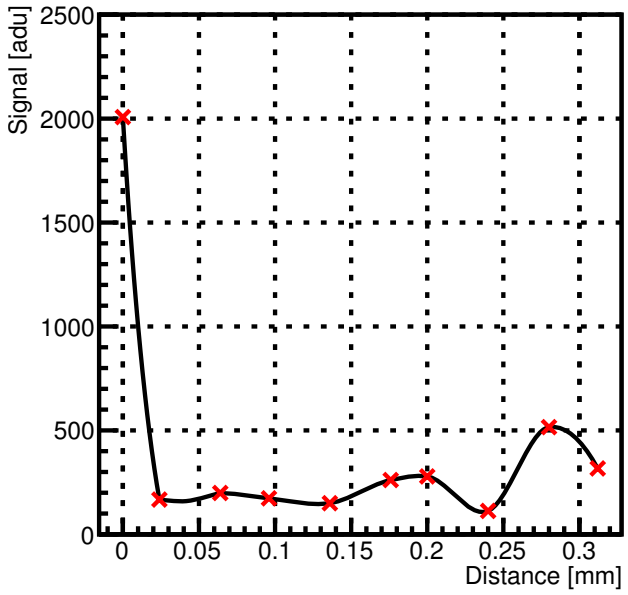

Figure 20.: Signal distribution along path for trajectory depicted in fig. 18.

Eventually the algorithm has calculated a delta trajectory which allows (among other things) to calculate the distribution of the deposited charge along the delta trajectory; this is shown in figure 20 for the trajectory depicted in figure 18.

Parameters like the total charge along the path, the physical path length and others can be used to calculate the distributions of these values for all delta events found. These distributions can then be used to compare the behaviour of delta electrons in different data samples. Due to the statistical nature of the elementary physical processes it is not meaningful to compare single events from different samples directly but distributions of certain variables (like the aforementioned) allow comparison. Usually these variables are based on a certain feature of the physical appearance and are thus called **shape variables**.

Escaping Delta Electrons: Due to the fact that the DEPFET sensor area is finite one has to keep in mind that a delta trajectory may escape the active area. Although this is unfortunate – as it results in loss of information – we assume that the influence of such events is rather low and can be compensated by using a sufficiently large data sample. However, when calculating e. g. the total charge deposited by a delta electron the rare very long delta tracks are of crucial relevance as they define the high energy tail of such a distribution. Unfortunately they are also the ones most probable to escape the active sensor area.

6.1.3. Physical Interpretation

The properties of the delta electron trajectory calculated can be used to determine the physical quantities describing the event. We reason that for every delta electron that comes to rest within the detector it should be possible to find a BRAGG-peak (cf. section 2.1) therefore a check for existence of a BRAGG-peak could be used to determine whether a delta electron is fully contained in the active sensor area.

By determining the total signal value that has been matched to the delta electron one can estimate the transferred energy E_{loss} of the ionisation process that created the delta electron and thus the ejection angle θ. Using only delta electrons escaping the detector plane (i. e. delta electrons without a BRAGG peak at the end of their trajectory) one can use the combination of θ and L (i. e. the length of the delta trajectory) to calculate the creation depth z within the detector plane. These three quantities fully describe the ejection of the delta electron.

6.2. Delta Selection

The full set of events reconstructed using the program chain explained in section 4.2 is examined with regard to certain criteria to select delta events. Appendix A contains of list of the program options and thresholds used in the delta ray reconstruction and analysis.

Size Criterion: Due to the fact that a delta cluster is comprised of a normal telescope hit cluster with an additional delta track cluster segment (section 6.1.1) the most straightforward criterion for delta event selection is the cluster size i. e. the number of firing pixels in a cluster. Therefore the initial selection of delta event candidates is done by selecting all clusters whose size exceeds a certain threshold.

Telescope Track Hit Criterion: To reject false clusters (e. g. noise clusters) it is checked whether there is a telescope track existent for all delta cluster candidates. Therefore it is indispensable to match the telescope tracks existing for the current detector event to the active plane i. e. to calculate the telescope track hit on the DUA. The criterion requires that one of the telescope tracks must exhibit a fitted hit on the delta candidate's cluster area; the fitted hit point defines the starting point of all delta trajectories of the cluster. To ensure that the results of this check criterion are of high quality it is required that the χ^2 value of the track suffices a quality threshold.
It is reasonable to assume that the initial particle continues travelling through the telescope after setting the delta electron(s) free. Therefore the telescope track should continue after the plane the delta electron was created on. We use this fact to reject nuclear events because in case of a nuclear event the initial particle should be deflected by a large angle (thus the telescope track "ends" on the delta plane because the track finding algorithm cannot cope with this).

Cluster Merging: Finally it is checked whether any of the clusters found on the DUA for the current event ID can be merged i. e. whether two clusters are closer than a certain threshold. This copes with delta trajectories which exhibit a gap that is wider than two pixels in either direction because those type of clusters will be reconstructed as two separate clusters by the clustering processor (cf. section 4.2.3).

6.3. Track Reconstruction

The Delta Track algorithm is a signal based algorithm developed for calculating the track of a delta electron from the cluster charge distribution of the event. It is capable of determining multiple delta tracks – corresponding to multiple delta electrons – if there are any in a delta cluster. It performs very well (cf. section 6.3.2).

6.3.1. Operating Principle

The algorithm tries to find a possible trajectory (consisting of successive pixel coordinates) of the delta electron starting at the telescope track hit location. This is done iteratively such that in each iteration a new step is added to the trajectory and a single pixel (the end position of the previous iteration) is removed from the cluster data collection. Therefore for each iteration there is an **origin pixel** which corresponds with the pixel that was added to the trajectory in the previous step.
The most basic principle deployed by this algorithm is to check all existing nearest neighbour pixels of the current origin for their charge signal; a nearest neighbour pixel is one which shares either a side or an edge with the current origin. Then the algorithm selects the pixel with the largest signal to be the next step in the trajectory.
Nevertheless the actual algorithm cannot be described this simple: numerous subroutines and checks have been implemented to cope with different problematic situations (such as those explained in section 6.1.2) but they will not be explained in detail in this document.
It is noteworthy that the algorithm is restricted to steps in a forward cone with an angular width between 90 and 180° (direction is defined by the previous track step's direction). Furthermore to cope with gap situations the algorithm allows steps which do not connect nearest neighbours but this is only possible when a gap situation is found.
The distance between two steps which have not been reconstructed by the gap resolution routine is always either P or $\sqrt{2}P$ where P is the pixel pitch[18] i. e. exactly one pixel width in either direction or both directions. This allows to use the reconstructed delta trajectory

[18] Assuming square pixels, otherwise one can find the distances $P_x, P_y, \sqrt{P_x^2 + P_y^2}$.

to calculate the **charge path distribution** i. e. the distribution of deposited charge along the path or $Q(x_i, x_{i+1})$, where Q is the deposited charge between the track segments x_i and x_{i+1}.
Although one cannot compare the resulting distributions between modules or data samples due to the stochastic nature of this distribution, it is possible to define shape variables based on the distribution's shape.

6.3.2. Algorithm Efficiency

For testing purposes we have calculated the efficiency of the delta track algorithm. The efficiency ϵ is defined by the relation

$$\epsilon := \frac{N_{\text{fin}}}{N_\delta},$$

where N_δ is the number of selected delta events (i. e. the number of events which passed all selection criteria) and N_{fin} is the number of events for which one or more delta trajectories have been found and which have not been rejected by a veto criterion. It is important to note that one must ensure that events with multiple delta trajectories count only as one entry towards N_{fin}. The resulting efficiency diagram is shown in figure 21 on a per module basis and for the combined data set. Obviously the algorithm performs with a very good efficiency which fluctuates by approximately 1 % around a value of 95 %. We cannot identify any modules which perform badly and are very satisfied with the overall result.

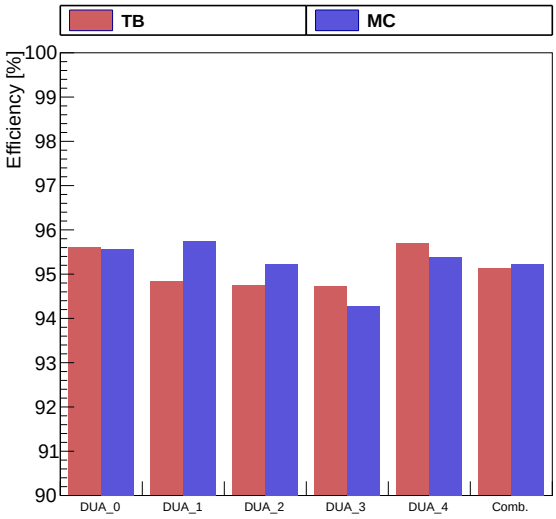

Figure 21.: Efficiency of the delta track algorithm.

7. Delta Electron Analysis

7.1. Delta Fraction

7.1.1. Definition

Possibly the most obvious criterion for the comparison of different sets of data is the **Delta Fraction** $\mathfrak{f}_\delta$ that is the percentage of delta hits among all valid hits. We have deemed a hit to be valid if a telescope track has been found for the corresponding plane hit. Therefore $\mathfrak{f}_\delta$ is defined by

$$\mathfrak{f}_\delta := \frac{N_\delta}{N_{\text{hit}}} .$$

To analyse the performance of the delta event selection process we have defined another quantity, called **Delta Size Fraction** $\mathfrak{f}_s$, which is defined by

$$\mathfrak{f}_s := \frac{N_s}{N_{\text{hit}}} .$$

where N_s is the number of hits which sufficed the cluster size criterion of the delta selection process. This criterion can be used to check whether there are many large clusters in the data sample which are eventually refuted as delta electron event.
Furthermore the delta fractions are a measure of the delta production rate and thus allow to evaluate the simulation of the production cross section.

7.1.2. Results

The resulting values for the two delta fractions are shown in the graph in figure 22. The discrepancies between TB and MC found for $\mathfrak{f}_\delta$ are in the order of one percent, which concurs with the discrepancy between modules in the experimental sample. Thus we conclude that the delta fraction $\mathfrak{f}_\delta$ is simulated accurately.
The size delta fraction $\mathfrak{f}_s$ differs by approximately two percent between experiment and MC

whereas the deviations between modules are in the order of one percent. The discrepancy is not very large, it is roughly twice the in-sample fluctuation, however, we are not certain how this discrepancy arises. Possible candidates are a wrong interaction cross section for the elementary physical process, faults in the delta electron creation (i. e. wrong/bad cut values) or "real life" effects (i. e. anything that has not been simulated but occurred in the actual data taking).

Despite the slight deviation in $\mathfrak{f}_s$ we are satisfied with the generation rate of the MC as the more significant fraction $\mathfrak{f}_\delta$ (which is of particular importance as the events comprising $\mathfrak{f}_\delta$ are the ones that were analysed further) is in very good agreement when comparing the two samples.

The errors shown are calculated using the assumption that the two components of the fractions are POISSON distributed and thus have a standard deviation which is equal to $\sqrt{N}$ where N is the value used for calculation. The error of the fraction entries has been calculated by propagating the individual errors i. e. the errors are estimated by

$$\sigma_{\mathfrak{f}_\delta} = \sqrt{\left(\frac{\sqrt{N_\delta}}{N_{\text{hit}}}\right)^2 + \left(\frac{\sqrt{N_{\text{hit}}}\cdot N_\delta}{N_{\text{hit}}^2}\right)^2} \qquad \text{and} \qquad \sigma_{\mathfrak{f}_s} = \sqrt{\left(\frac{\sqrt{N_s}}{N_{\text{hit}}}\right)^2 + \left(\frac{\sqrt{N_{\text{hit}}}\cdot N_s}{N_{\text{hit}}^2}\right)^2}.$$

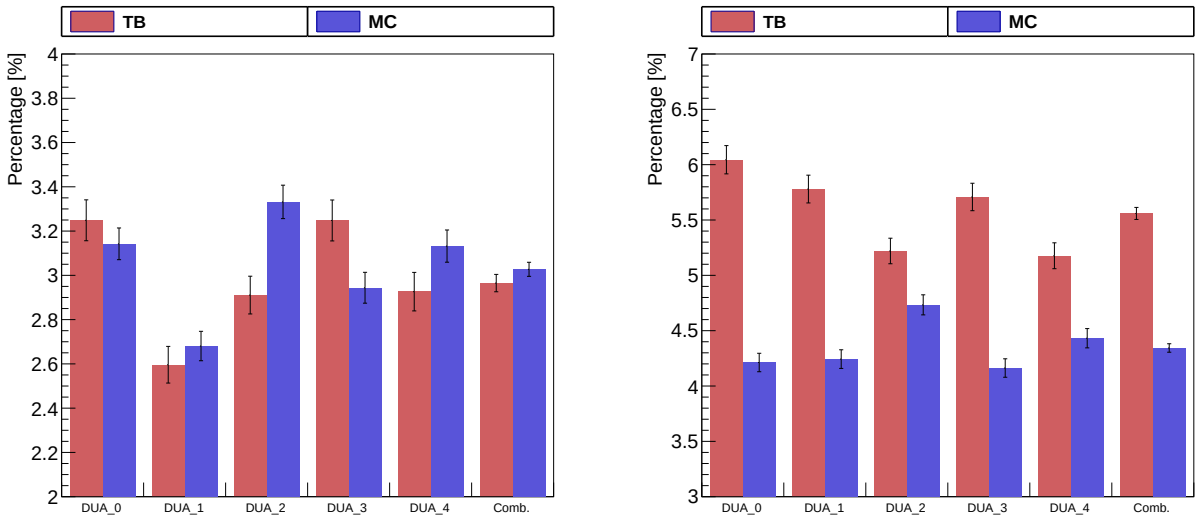

(a) Delta Fraction $\mathfrak{f}_\delta$ (b) Delta Fraction $\mathfrak{f}_s$

Figure 22.: Plot of delta fractions $\mathfrak{f}$ per DUA and combined.

7.2. Delta Track Length

The distribution of the track length

$$X := \sum_i x_i$$

for the combined data of all DUAs is given in figure 23 for the two data sources. The distributions show good agreement between TB and MC data. Taking a closer look we find that the number of short delta tracks is slightly larger for the TB data set, consequently we find slightly more long delta tracks in the MC sample.
The logarithmic plot in figure 23b shows a slight deviation between the data samples for very long delta trajectories, however, due to limited statistics, this might be a result of the small number of entries for large distances.

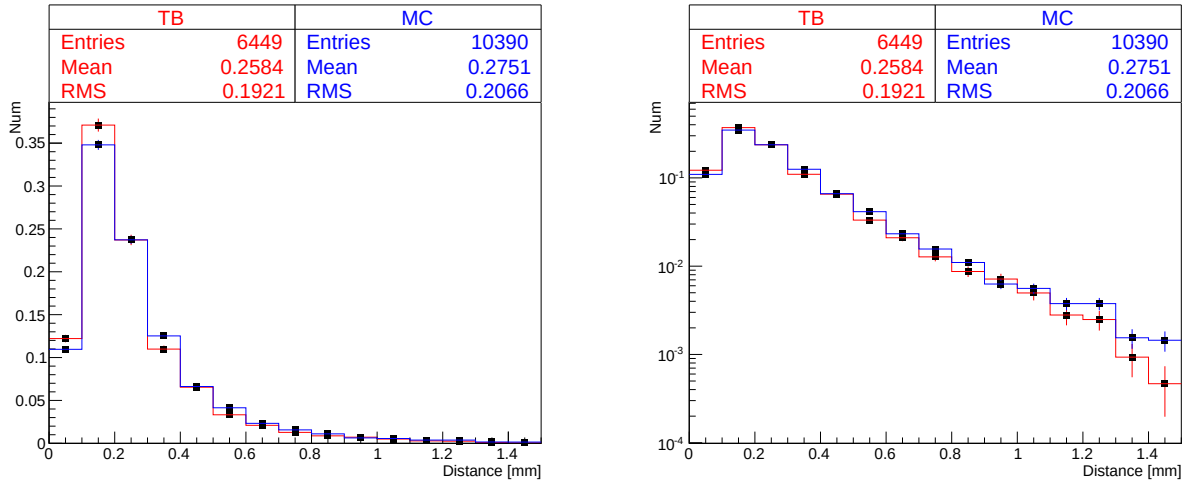

(a) Non-Logarithmic Plot (b) Logarithmic Plot

Figure 23.: Distribution of the delta track length using the combined data of DUAs *0* to *4*. Distributions have been normalised to an area equal to unity.

The errors of the distribution entries as shown are statistical errors which have been calculated by the ROOT framework [9].

7.3. Line Likeness

7.3.1. Definition

The **Line Likeness** L is a criterion which represents the deviation of the calculated delta trajectory from a straight line between start and endpoint. It can be used to compare the

experimental and MONTE-CARLO data. It is defined by the relation

$$L := \frac{X}{\sum_{i=1}^{n} x_i},$$

where x_i are the distances of the n track segments which constitute the delta trajectory and X is the distance between the first and last point of the delta trajectory. Due to the fact that the delta trajectory trajectory is always longer or of equal length when compared with the straight line between start and endpoint, L is in the range $]0:1]$. The inverse line likeness, which is defined as $L^{-1} := \frac{1}{L}$, is always larger or equal to one.
This variable represents the result of the scattering processes a delta electron undergoes because each scattering process results in a small deflection which in turn increases the trajectory's length and thus decreases L.
Figure 24 shows an example of an event with a considerably small line likeness. Obviously the delta trajectory is curled and the delta electron has been deflected several times by a large angle, the resulting value for L is thus a lot smaller than unity.

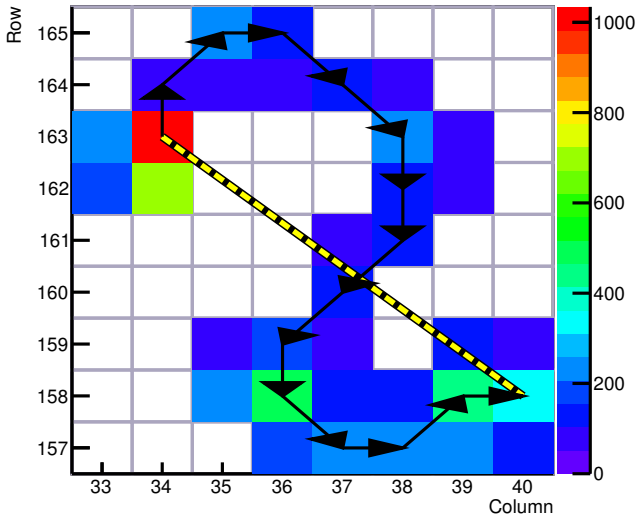

Figure 24.: Example application of the line likeness shape variable, event taken from the test beam data. Line likeness has been calculated to be $L \approx 0.48$. Delta trajectory shown as black arrows, straight line for line likeness calculation shown as dashed, yellow line.

The principle of relating true path length and geometrical path length is very similar to the concept deployed by `Geant4` for the calculation of the effects of MSC [11].

7.3.2. Results

Figure 25 shows the distributions of the line likeness for the two data samples using the data from all modules. The distributions for the individual modules show similar shape, however, we note that no significant difference is visible between the distributions for module *2* and the others, thus we assume that the line likeness is independent of the pixel pitch for the modules used in the analysis.

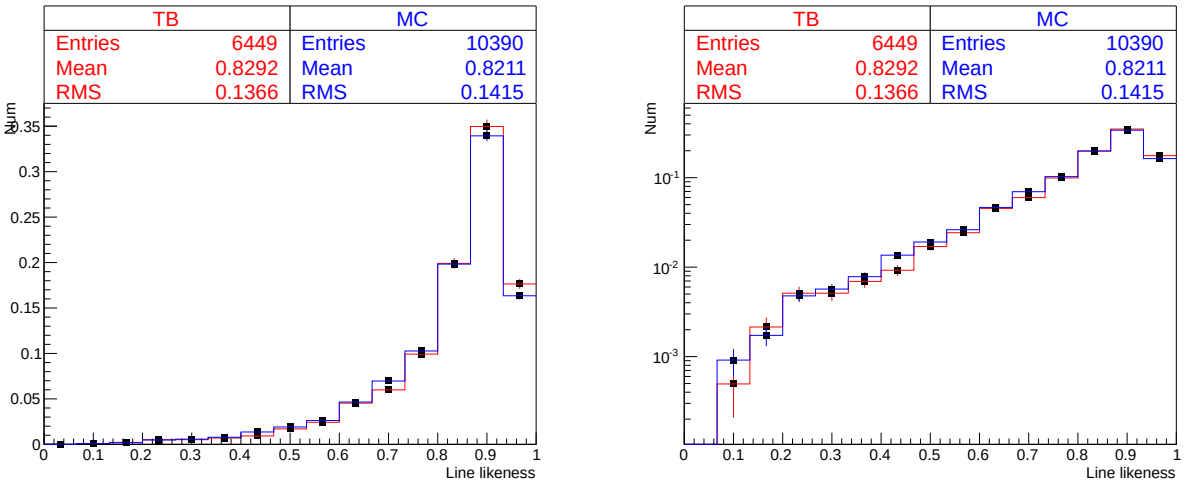

(a) Non-Logarithmic Plot

(b) Logarithmic Plot

Figure 25.: Plot of the distributions of the line likeness using combined data from all modules for the two data samples. Area has been normalised to unity.

We find that the distributions are in very good agreement for a line likeness larger than 0.6, for smaller values slight deviations between the distributions are visible. These deviations may stem from the small number of data points available for very low line likenesses. This in turn is a result of the definition of the line likeness because for a small line likeness the difference between straight line and delta trajectory must be very large, which is only possible (or plausible) for very long delta trajectories, which are rare.
The maximum value of the distribution is different from unity, therefore we find that a slight deviation from a straight line is more probable than the straight connection.
The errors of the distribution entries as shown are statistical errors which have been calculated by the `ROOT` framework [9].

7.4. Truncated Mean Analysis

The truncated mean descriptor (cf. [4]) has been explained and demonstrated in detail in section 2.5, we have applied the method to the data samples using different values for the cut percentage p. The distributions for different values of p show a similar behaviour when compared to the results of the example analysis shown in section 7.4 i. e. the maximum remains approximately at the same location whereas the width of the distribution decreases with rising p. For the sake of a larger statistic we compare only the distributions of the combined data from all modules. Figure 26 shows the distributions of the truncated mean descriptor for $p = 10$ and 15 %.
The distribution shows the calculated most probable energy loss of a delta electron in the detector plane. As expected we see a sharp cut on the left side, smeared by the experimental

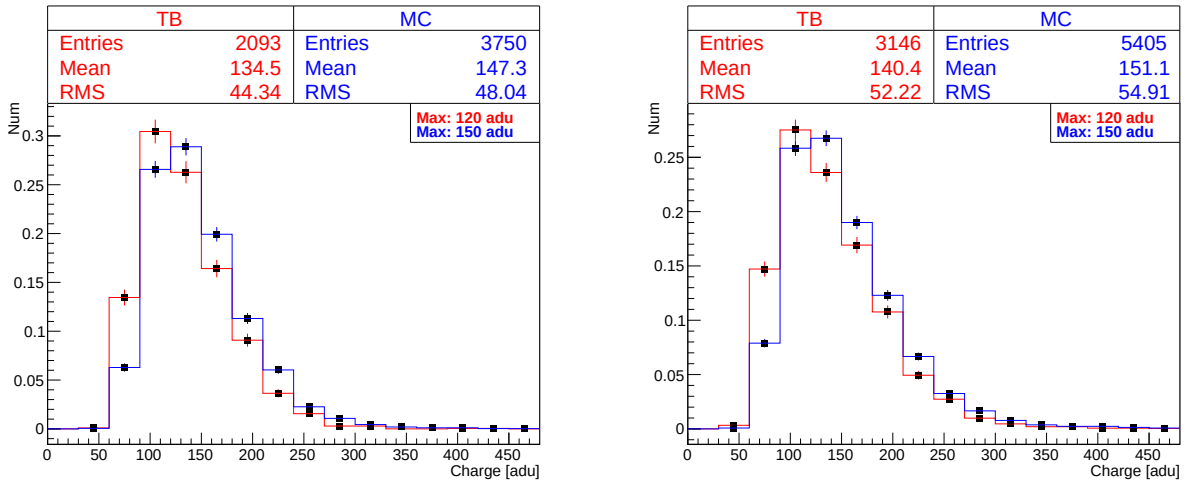

(a) $p = 10\,\%$ **(b)** $p = 15\,\%$

Figure 26.: Distributions of the truncated mean descriptor $C^{(p)}$ for $p = 10,\ 15\,\%$, combined data from all modules was used and the distribution's area was normalised to unity. The errors of the distributions are statistical errors calculated by the ROOT framework [9].

uncertainties. This cut corresponds with the minimal energy that can be deposited by a travelling delta electron and still measured.

Minimal Charge: Under the assumption that the deviation from the maximum of the distribution towards lower charge values is based purely on experimental smearing we can estimate the minimal deposited charge by the signal value of the peak.
This minimal signal value can be transformed into a electron charge value using the charge calibration factors from 5.2, afterwards we can estimate the corresponding E_{loss} value using the ionisation yield relation given by equation 4. Naturally this must be done using the per module distributions as the calibration factors differ between modules.
With the knowledge of the distance over which this energy has been deposited we can calculate the corresponding $\frac{\mathrm{d}E}{\mathrm{d}x}$. This has been done and the resulting $\frac{\mathrm{d}E}{\mathrm{d}x}$ values are between 1.44 and $1.62\,\mathrm{MeVcm^2g^{-1}}$; different values stem from different modules and cut percentages p. Due to the large error of the minimal charge selection (which is in the order of a bin width i. e. $\approx 25\,\mathrm{adu}$ and transforms to a value of $\sigma_{\frac{\mathrm{d}E}{\mathrm{d}x}} = 0.32\,\mathrm{MeVcm^2g^{-1}}$ assuming this error energy was deposited over a distance of one pixel pitch $P = 24\,\mu\mathrm{m}$) the two values spanning the above range are consistent with each other.
When comparing the averaged value[19] $\frac{\mathrm{d}E}{\mathrm{d}x}_{\mathrm{Avg}} = 1.53 \pm 0.45$ to the function of the Bethe-Bloch formula shown in figure 2 one can identify the minimal deposited charge per unit length to be equal to the $\frac{\mathrm{d}E}{\mathrm{d}x}$ value deposited by the MIP i. e. a $\beta\gamma$ value of the delta electron of ≈ 3.
It is important to note that this calculation is a) heavily approximated and b) wrong, due

[19] Error has been propagated.

to the fact that the BETHE-BLOCH formula cannot be used to describe the energy loss of electrons. Nevertheless we have performed the analysis to grasp an estimate of the actual value; the result calculated above must be used with caution.

Single Landau Analysis: The above analysis is performed by calculating the truncated mean absolute value per event and comparing the per-module distribution between different data samples. A more obvious approach is to calculate the actual straggling function $f(\Delta, x)$ (i. e. the pdf of the deposited energy) for a single event, do a LANDAU fit and analyse the result. This approach can only work for events with a large number of entries i. e. a very long delta trajectory. We have performed a cut, selecting the ten events with the longest delta track per module. For each entry of this subset we calculated the truncated set (i. e. we have removed three values at start and end of the trajectory to overcome the influence of telescope track and BRAGG peak and afterwards removed elements as described in section 2.5) and performed a LANDAU fit.

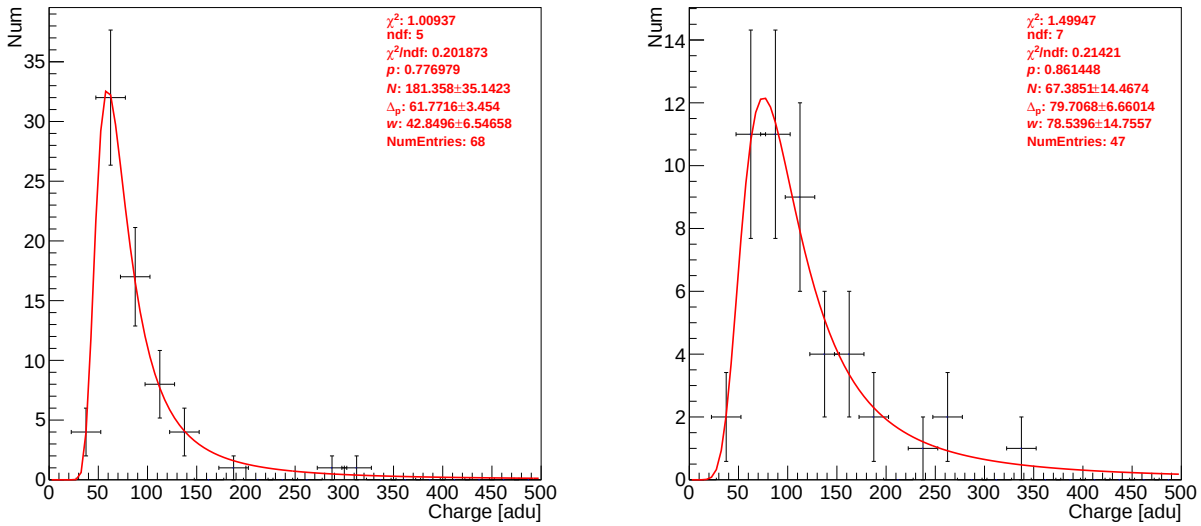

(a) TB: $p = 10\,\%$ **(b)** MC: $p = 10\,\%$

Figure 27.: Plots of selected single LANDAU distributions for cut percentage $p = 10\,\%$. A LANDAU fit (binned fit) was performed using the ROOT framework [9], the fit parameters are listed in the figure: N is a normalisation coefficient, Δ_p is the MPV and w is the distribution's width. The p value was calculated from the χ^2 and ndf value using the ROOT framework. The errors in x-direction are estimated by the noise value of 15 adu the errors in y direction are statistical errors calculated by the ROOT framework.

Figure 27 shows two selected single LANDAU plots, one for each data sample. Of all events on which this method was executed the above two are of the best quality. One can find a very good agreement between the data points and the fit function, these plots can be used to identify the quantities Δ_p and w which are the statistical parameters of the underlying straggling function.

Using a larger data sample it might be possible to perform this analysis on a far greater

number of events and thus calculate the per-run distributions of Δ_p and w. However, it is to note that of the 100 events selected for the single LANDAU method approximately 30 % yielded good results. This leads us to the conclusion that one must use a data sample many times larger than the one used in this analysis to be able to evaluate the single LANDAU method statistically.
The single LANDAU plots allow to assess the Signal-To-Noise ratio of the MPV i. e. the S/N of the typical energy deposition of a delta electron per unit path length. For figure 27a we find that the S/N is ≈ 4. This allows conclusion that the measurement and analysis of the delta electron trajectories has been enabled by the very good noise profile of the DEPFET.

7.5. Bragg Peak Analysis

7.5.1. Procedure

In the course of the thesis we have experimented with different criteria to determine whether a delta track exhibits a BRAGG peak and how to determine the resulting BRAGG charge i. e. the (total) signal deposited in the BRAGG peak. Eventually two methods have been selected and are presented below.

Cut Based Approach: The most straightforward approach is a cut based approach: We define a 3×3 area[20] centred to the final step of the calculated delta trajectory. In case that the total signal in this area exceeds a threshold S_{BRAGG} we designate the track to have a BRAGG peak whose charge equals the total signal in the 3×3 area.
To ensure that this is not corrupted by the telescope track main cluster we require that the centre of the 3×3 area is more than six pixel distant from the telescope track hit in either direction.

Track Based Approach: Another method is to use the calculated delta track data to search for and identify a possible BRAGG peak. The first step for this procedure is to identify all peaks (i. e. local maxima) in the track charge distribution.
Afterwards the collection of peaks is traversed backwards (i. e. starting at the last step of the trajectory) in search for a semi-global maximum. This semi-global maximum is defined to have a certain minimal vertical extent ΔS, furthermore both its flanks must descend to a value below a certain threshold. This ensures that the semi-global maximum is a peak of

[20] Of course other area sizes may be chose e. g. size 5×5 showed promising results, however, when manually checking the event displays of delta trajectories we decided to use the smaller field because – when checked manually – this area contained the whole BRAGG charge in most cases.

sufficient height and extends above a lower non-BRAGG ionisation level.
It is permitted that the resulting BRAGG peak is comprised of smaller peaks as long as the above criteria are fulfilled for the combined set of values; this compensates for small fluctuations in the deposited energy. To compensate for the large peak at the start of the trajectory (resulting from the large signal deposited in the telescope track hit cluster) it is required that the calculated BRAGG peak extends no closer than two pixels to the first minimum of the charge distribution (we assume that the first minimum corresponds with the low end of the flank of the peak from the telescope track hit cluster).

7.5.2. Results

Cut Based Approach: The cut based analysis has been deployed using the thresholds $S_{\text{BRAGG}} = \{500, 700, 900\}$ adu; the resulting distributions of the percentages can be found in figure 28.

The total discrepancies between the sets of data are in the order of $\approx 8\,\%$ for $S_{\text{BRAGG}} = 500$ and 700 adu; the flucations for different modules in the same sample are in the order of $\approx 4 - 6\,\%$ for these thresholds. That is to say we find discrepancies between TB and MC samples although we cannot tell for sure whether those discrepancies are consistent with the ordinary fluctuations. Nevertheless we find the tendency that the MC sample includes more delta tracks with a BRAGG peak, as all but one data set (for $S_{\text{BRAGG}} = 500$ adu, DUA *2*) exhibits this behaviour.
For $S_{\text{BRAGG}} = 900$ adu we find similar discrepancies but more importantly we find that the test beam data set for DUA *2* contains by far less events with a BRAGG peak than the MC sample. Due to the fact that the percentage of BRAGG peak events for the TB sample of DUA *2* for $S_{\text{BRAGG}} = 500$ and 700 adu is once larger and once very close to the value of of the corresponding MC sample entry we can assume that the TB sample for DUA *2* contains an unusual high number of events whose BRAGG charge is in the proximity of 500 adu but fewer clusters with a larger BRAGG charge.
The fact that we find this behaviour in the experimental data leads us to the conclusion that the discrepancies in the number of BRAGG events are purely based on fluctuations and not based on faulty simulation.
The errors shown are calculated in the same way (and under the same assumption i. e. that the components of the quantity depicted are POISSON distributed) as the errors of the delta fractions, cf. section 7.1.2 for further explanation.

Track Based Approach: Figure 29a shows the BRAGG charge distribution for DUA *4* as calculated using the track based approach to the BRAGG peak determination. Clearly the

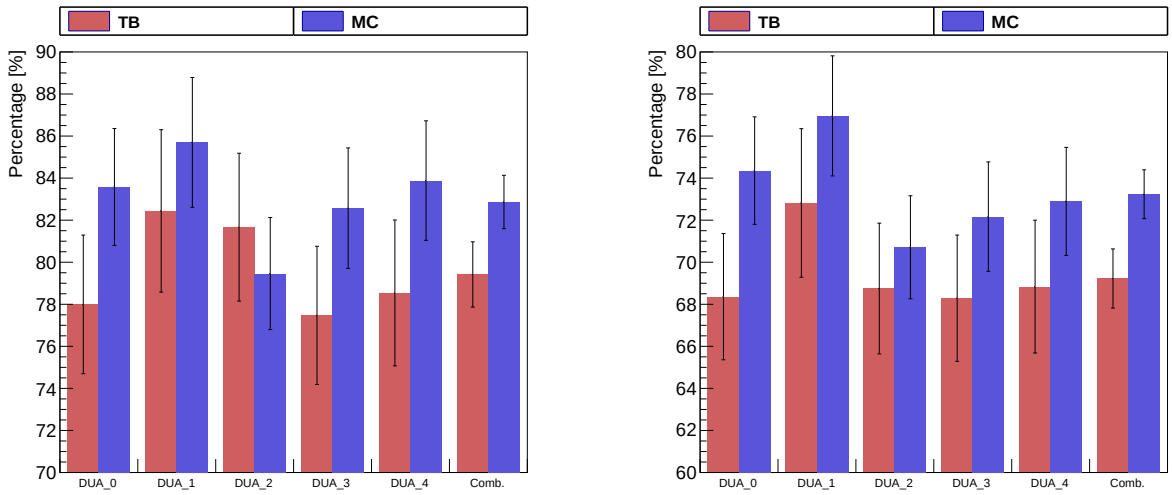

(a) $S_{\mathbf{Bragg}} = 500\,\mathrm{adu}$ **(b)** $S_{\mathbf{Bragg}} = 700\,\mathrm{adu}$

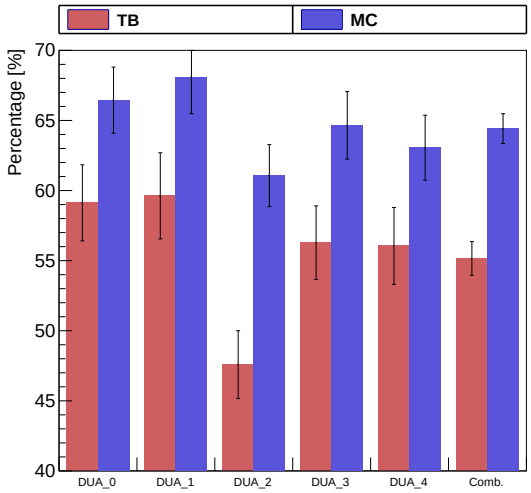

(c) $S_{\mathbf{Bragg}} = 900\,\mathrm{adu}$

Figure 28.: Percentage of delta events which have been found to have a BRAGG peak using different signal thresholds S_{BRAGG}; percentage is given in relation to total number of delta events.

two distributions are of similar shape, however, the distribution for the TB sample exhibits a larger peak and is narrower (has a lower tail). This behaviour can be found similarly in the distributions of the other modules. The discrepancies between experimental data and MC data are for some bins in the order of the smaller value of the two distributions for that bin, thus we are uncertain whether the distributions match well.

The percentages of events identified to have a BRAGG peak – shown in figure 29b – yield a similarly inconclusive result. The discrepancies between modules within a sample is approximately 3 % for the MC and 12 % for the TB sample; the deviations between the two samples are in the order of the discrepancies between modules in the TB sample. Therefore this analysis criterion does not allow to evaluate the performance of the MC as the in-sample

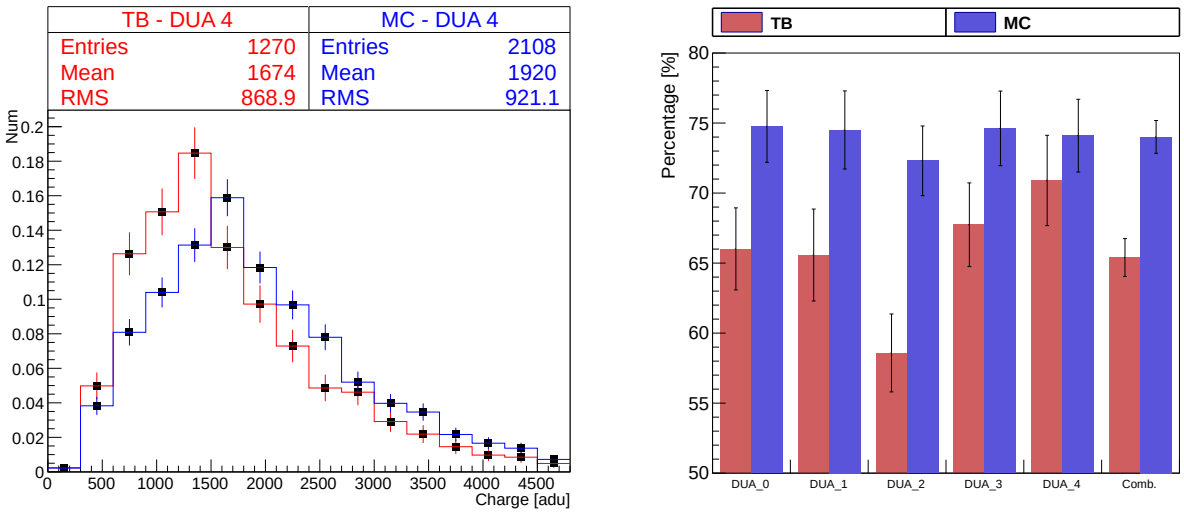

(a) DUA *4* **(b)** Statistics

Figure 29.: Fig. 29a: Distribution of BRAGG charge for DUA *4*, area of distributions has been normalised to unity; fig. 29b: percentage of events with BRAGG peak on per module basis and for the combined data sample.

fluctuations are of the same order as the fluctuations between different samples.
With 12 % those fluctuations are very high which leads us to the conclusion that the performance of the track based analysis must be further improved prior to using this criterion for the quality assessment of the MC simulation.
The errors shown in figure 29a are calculated as statistic errors by the ROOT framework [9], the errors in figure 29b have been calculated using the same method as the errors of the delta fraction (cf. section 7.1.2).

In conclusion we find that the BRAGG peak analysis has come to inconclusive results and must be further improved to be able to make a clear statement. However, we would like to point out that the criteria used for analysis probably can yield more conclusive results when the analysis is fine-tuned.

8. Conclusion and Outlook

The development of a strict set of criteria for the selection of a pure sample of delta electron events and an algorithm for the reconstruction of the trajectory of a delta electron has been a great success. Our selection method ensures that the sample is very pure and removes the problem of false hit reconstruction of the telescope track hit. The algorithm developed for delta track reconstruction has a very good efficiency (cf. figure 21) and is able to cope with numerous different problematic situations such as in-track gaps, harsh turns, heavily curled tracks and many more. Furthermore we have been able to develop several shape variables of high quality which have been used to compare the data samples.

Due to the high quality delta track reconstruction we are able to resolve any observable (i. e. shape variable) as function of the track length l or position x along the track. This allows detailed analysis of the delta electron's behaviour as a process which is evolving along a path. We found that the delta electron production rate found for the experimental sample is compliant with the simulated sample (see figure 22). Furthermore the distribution of delta track lengths is in very good agreement between the two data samples (cf. figure 23). Therefore we can conclude that the single collision cross section used by the simulation model is in very good agreement with reality.

The analysis of the delta electron straggling (discussed in section 7.4) has shown that the delta electron behaves like a Bethe-Bloch MIP. We found that the actual straggling function calculated for single events (titled "single Landau method") can be approximated with a Landau function with very good agreement; this supports the argument presented in section 2.1.

Lacking a criterion for validating the effects of multiple scattering we have developed the line likeness shape variable which shows good agreement of the two data samples. It relates true and geometric path lengths which depend on the deflection due to multiple scattering, however, the actual deflection process cannot be validated with the line likeness alone. The Bragg peak analysis allows a preliminary validation of the simulation, however, it must be

enhanced and developed further for a more thorough result.

It is important to note that the LANDAU and BETHE-BLOCH theory is actually not valid for electrons, thus the analysis performed cannot be used to calculate the actual kinematic variables of the delta electron (as was done in section 7.4). The above theories can be used for heavy particles but not electrons. Electron behaviour is described by the BERGER-SELTZER formula and the production of delta electrons is usually calculated as MÖLLER scattering [11]. Although it is excluded in the energy range of the delta electrons analysed it is important to note that the process of *bremsstrahlung* must be carefully distinguished from delta electron production. The qualitative analysis done in this thesis is exact, however, the quantitative calculation of kinetic variables such as done in 7.4 cannot yield correct results.

We have found that a good detector simulation (not only of the physical processes but of the digitiser stage too) is of great importance. The digitiser yields data which are equivalent to the experimental sample and can be processed by the very same reconstruction chain (when using the calibration factors described in section 5.2).

Using the analysis and reconstruction methods developed in this thesis we can calculate the practical ranges of delta electrons with much higher precision than the listing by BICHSEL in table 1. By calculating the total signal deposited in a delta track this calculation is possible without the use of the more complex BERGER-SELTZER and MÖLLER theory described above.
In this thesis we have not assessed the shape of the delta clusters, however, the data sample extracted by this analysis can be analysed for this criterion with ease once a valid shape variable has been developed.
The analysis of the BRAGG peak might be used to determine which delta electrons remain in the sensitive area (i. e. are fully measured) and thus allow to reject any escaping delta electron. Furthermore it is possible to calculate the delta electron's kinematic variables using the BRAGG peak charge only as this is a measure of the delta electron's momentum.
The line likeness allows a preliminary check of the agreement of experiment and simulation with regard to the effects of multiple scattering. However, a subsequent analysis should implement a criterion based on the curvature of the delta trajectory. One possible approach is the usage of splines for the interpolation of the delta trajectory; the splines can afterwards be used to calculate a variety of shape variables.

A. Reconstruction Parameters

In this appendix the relevant steering parameters of the reconstruction chain and subsequent analysis are listed along with their values.

- **Pedestal and Noise Calculation:**
  - Assumed noise fluctuation value: 15 adu (TB) or 280 e^- (MC)
  - Assumed pedestal value: 0 adu (TB) or 0 e^- (MC)
- **Zero Suppression:**
  - Minimum signal value not assumed to be zero, in units of S/N (signal-to-noise ratio): 3
- **Clustering:**
  - Allowed that nearest neighbours may be separated by a one pixel gap (cf. section 4.2.3).
  - Minimum signal for a cluster not to be rejected; in units of S/N: 7
  - Minimum signal for the seed pixel (i. e. pixel with largest signal) of a cluster; in units of S/N: 5
- **Hit Reconstruction:**
  - Allows "bad" clusters i. e. clusters which are close to the detector's border.
- **Alignment:**
  - Alignment tracks must have residual less than 500 µm.
  - χ^2 for alignments tracks must be less than 1000.
  - Tracks may not skip any modules i. e. there must be six hits per track.
- **Track Reconstruction:**
  - Alignment tracks must have residual less than 300 µm.
  - χ^2 for alignments tracks must be less than 1000.
  - There must hit at least four modules and a skip may not be larger than one module.
- **Delta Ray Reconstruction:**
  - A delta trajectory may exhibit a gap which is not larger than five pixels (i. e. three missing pixel in either direction).
  - The total cluster charge for a delta event may not exceed 20000 adu (value in units e^- can be calculated on per module basis using the values listed in table 3).

- A maximum number of seven pixels may remain in a cluster after all delta track entries have been removed from the cluster data.
- The maximum distance between two separate clusters which will be merged to a common delta cluster may not exceed five pixels (i. e. five missing pixels).
- The minimum cluster size for a delta cluster candidate must be equal to or more than 12 pixels.
- A possible delta cluster fragment for merging must at least be four pixels large.
- The telescope track corresponding to a delta hit must have a hit on the plane after the DUA.

B. Bibliography

[1] L. Rossi, P. Fischer *et al.* *Pixel Detectors: From Fundamentals to Applications*. Particle Acceleration and Detection. Springer, **2010**. ISBN 9783642066528.

[2] W.R. Leo. *Techniques for Nuclear and Particle Physics Experiments: A How-To Approach*. Springer, **1994**. ISBN 9783540572800.

[3] K. Kleinknecht. *Detektoren für Teilchenstrahlung*. Teubner Studienb Cher Physik. Teubner, **2005**. ISBN 9783835100589.

[4] Hans Bichsel. *A method to improve tracking and particle identification in TPCs and silicon detectors. Nuclear Instruments and Methods in Physics Research Section A: Accelerators, Spectrometers, Detectors and Associated Equipment*, **562**, 1:pp. 154 – 197, **2006**. ISSN 0168-9002. doi:10.1016/j.nima.2006.03.009. URL http://www.sciencedirect.com/science/article/pii/S0168900206005353.

[5] K Nakamura, K Hagiwara *et al.* *Review of Particle Physics, 2010-2011. Review of Particle Properties. J. Phys. G*, **37**, 7A:p. 075021, **2010**.

[6] C. Grupen. *Teilchendetektoren*. BI-Wissenschaftsverlag, **1993**. ISBN 9783411165711.

[7] L. Landau. *On the energy loss of fast particles by ionization. J.Phys.(USSR)*, **8**:pp. 201–205, **1944**.

[8] R Mori, M Bruzzi *et al.* *Charge collection measurements on slim-edge microstrip detectors. Journal of Instrumentation*, **7**, 05:p. P05002, **2012**. URL http://stacks.iop.org/1748-0221/7/i=05/a=P05002.

[9] *ROOT: A Data Analysis Framework*. URL http://root.cern.ch/.

[10] H. Bethe. *Zur Theorie des Durchgangs schneller Korpuskularstrahlen durch Materie. Annalen der Physik*, **397**, 3:pp. 325–400, **1930**. ISSN 1521-3889. doi:10.1002/andp.19303970303. URL http://dx.doi.org/10.1002/andp.19303970303.

[11] *Geant4 Physics Reference Manual*. URL http://geant4.web.cern.ch/

geant4/UserDocumentation/UsersGuides/PhysicsReferenceManual/fo/PhysicsReferenceManual.pdf.

[12] Kati Lassila-Perini and László Urbán. *Energy loss in thin layers in GEANT. Nuclear Instruments and Methods in Physics Research Section A: Accelerators, Spectrometers, Detectors and Associated Equipment*, **362**, 2–3:pp. 416 – 422, **1995**. ISSN 0168-9002. doi:10.1016/0168-9002(95)00344-4. URL http://www.sciencedirect.com/science/article/pii/0168900295003444.

[13] C. Geisler. *Performance Study of DEPFET Pixel Detector Prototypes for Future Lepton Colliders Conducted at Beam Tests*, **2010**. URL http://physik2.uni-goettingen.de/research/high-energy/publications/DiplomGeisler.pdf.

[14] A. Ribon. *Validation of Geant4 and Fluka Hadronic Physics with Pixel Test-Beam Data*. Technical Report CERN-LCGAPP-2004-009, CERN, **2004**. URL http://lcgapp.cern.ch/project/docs/notePixelStudy.pdf.

[15] D. Barberis, M. Cervetto and B. Osculati. *Hadronic Interactions in Pixel Detectors*. Technical Report ATL-PHYS-2003-021. ATL-COM-PHYS-2002-015, CERN, Geneva, **Apr 2002**. Revised version number 1 submitted on 2003-07-16 10:44:25.

[16] N. Wermes. *Pixel Vertex Detectors. ArXiv Physics e-prints*, **November 2006**. arXiv:physics/0611075.

[17] E. J. Kobetich and Robert Katz. *Energy Deposition by Electron Beams and δ-Rays. Phys. Rev.*, **170**:pp. 391–396, **Jun 1968**. doi:10.1103/PhysRev.170.391. URL http://link.aps.org/doi/10.1103/PhysRev.170.391.

[18] J. Kemmer and G. Lutz. *New detector concepts. Nuclear Instruments and Methods in Physics Research Section A: Accelerators, Spectrometers, Detectors and Associated Equipment*, **253**, 3:pp. 365 – 377, **1987**. ISSN 0168-9002.

[19] T. Abe, I. Adachi *et al.* (Belle Collaboration). *Belle II Technical Design Report. ArXiv e-prints*, **November 2010**. 1011.0352.

[20] J.J. Velthuis, Z. Drasal *et al. A DEPFET Based Beam Telescope With Submicron Precision Capability. Nuclear Science, IEEE Transactions on*, **55**, 1:pp. 662 –666, **feb. 2008**. ISSN 0018-9499. doi:10.1109/TNS.2007.914031.

[21] P. Kodyš *et al. Intrinsic resolutions of DEPFET detector prototypes measured at beam tests. Nuclear Instruments and Methods in Physics Research Section A: Accelerators, Spectrometers, Detectors and Associated Equipment*, **638**, 1:pp. 24 – 32, **2011**. ISSN 0168-9002. doi:10.1016/j.nima.2011.02.015.

[22] W Neeser, M Böcker *et al.* *DEPFET–a pixel device with integrated amplification.* *Nucl. Instrum. Methods Phys. Res., A*, **477**, 1-3:pp. 129–136, **2002**.

[23] C. Marinas. *The ILC DEPFET Prototype: Report of the Test Beam at CERN 2008.* *ArXiv e-prints*, **January 2009**. 0901.4639.

[24] P. Fischer, W. Neeser *et al.* *Readout concepts for DEPFET pixel arrays.* *Nucl.Instrum.Meth.*, **A512**:pp. 318–325, **2003**. doi:10.1016/S0168-9002(03)01909-0. hep-ex/0209074.

[25] C. Marinas (DEPFET Collaboration). *The Belle II DEPFET vertex detector: Current status and future plans.* *JINST*, **7**:p. C02029, **2012**. doi:10.1088/1748-0221/7/02/C02029.

[26] S. Furletov (DEPFET Collaboration). *The Belle II pixel vertex detector.* *JINST*, **7**:p. C01014, **2012**. doi:10.1088/1748-0221/7/01/C01014.

[27] *The ILCSoft Software Framework Homepage.* URL http://ilcsoft.desy.de/.

[28] R. Frühwirth. *Application of Kalman filtering to track and vertex fitting.* *Nuclear Instruments and Methods in Physics Research Section A: Accelerators, Spectrometers, Detectors and Associated Equipment*, **262**, 2–3:pp. 444 – 450, **1987**. ISSN 0168-9002. doi:10.1016/0168-9002(87)90887-4.

[29] R. Frühwirth, T. Todorov and M. Winkler. *Estimation of detector alignment parameters using the Kalman filter with annealing.* *Journal of Physics G: Nuclear and Particle Physics*, **29**, 3:p. 561, **2003**.

[30] V. Karimäki, T. Lampén and F.-P. Schilling. *The HIP Algorithm for Track Based Alignment and its Application to the CMS Pixel Detector.* Technical Report CMS NOTE-2006/018, CERN, **2006**.

[31] *Mokka.* URL http://ilcsoft.desy.de/portal/software_packages/mokka/.

[32] *Geant4: A toolkit for the Simulation of the Passage of Particles through Matter.* URL http://geant4.cern.ch/.

[33] Zbynek Drasal, Kolja Prothmann and Benjamin Schwenker. *Silicon Simulation Code For Belle II & ILC.* In *The 20th Anniversary International Workshop on Vertex Detectors.* Proceedings of Science, **2011**.

C. Acknowledgements

First of all I would like to thank Prof. Dr. Ariane Frey for giving me the opportunity to write my bachelor thesis in particle physics and naturally for being the first referee of the thesis. It has been a most interesting experience to be working as colleague among the fellow scientists in her research group. I would like to express my special thanks for giving me the opportunity to work at a test beam session and experience the rush of a restricted time slot at a major research facility.
Furthermore I would like to thank P. D. Dr. Jörn Grosse-Knetter for being the second referee of my thesis.
I wish to offer my gratitude to my adviser Dipl. Phys. Benjamin Schwenker for his helpful comments and the fruitful discussions we had whenever a problem arose. The tremendous effort and patience he invested and the helping hand he was able to offer cannot be appreciated enough. It has been a satisfying experience to work along his side.

Erklärung nach §13(8) der Prüfungsordnung für den Bachelor-Studiengang Physik und den Master-Studiengang Physik an der Universität Göttingen:

Hiermit erkläre ich, dass ich diese Abschlussarbeit selbständig verfasst habe, keine anderen als die angegebenen Quellen und Hilfsmittel benutzt habe und alle Stellen, die wörtlich oder sinngemäß aus veröffentlichten Schriften entnommen wurden, als solche kenntlich gemacht habe.
Darüberhinaus erkläre ich, dass diese Abschlussarbeit nicht, auch nicht auszugsweise, im Rahmen einer nichtbestandenen Prüfung an dieser oder einer anderen Hochschule eingereicht wurde.

Göttingen, den 29. Juli 2012

(Fabian Wilk)